

Article

Zn-Cr Layered Double Hydroxides for Photocatalytic Transformation of CO₂ under Visible Light Irradiation: The Effect of the Metal Ratio and Interlayer Anion

Dolores G. Gil-Gavilán ¹, Daniel Cosano ¹, Juan Amaro-Gahete ¹, Miguel Castillo-Rodríguez ², Dolores Esquivel ¹, José R. Ruiz ^{1,*} and Francisco J. Romero-Salguero ^{1,*}

¹ Departamento de Química Orgánica, Instituto Químico para la Energía y el Medioambiente (IQUEMA), Facultad de Ciencias, Universidad de Córdoba, Campus de Rabanales, Edificio Marie Curie, 14071 Córdoba, Spain; q52gigad@uco.es (D.G.G.-G.); q92cohid@uco.es (D.C.); q22amgaj@uco.es (J.A.-G.); q12esmem@uco.es (D.E.)

² Departamento de Física Aplicada, Radiología y Medicina Física, Universidad de Córdoba, Campus de Rabanales, 14071 Córdoba, Spain; mcastillo1@uco.es

* Correspondence: qo1ruarj@uco.es (J.R.R.); qo2rosaf@uco.es (F.J.R.-S.); Tel.: +34-957-218355 (F.J.R.-S.)

Abstract: Carbon dioxide is the main gas responsible for the greenhouse effect. Over the last few years, the research focus of many studies has been to transform CO₂ into valuable products (CO, HCOOH, HCHO, CH₃OH and CH₄), since it would contribute to mitigating global warming and environmental pollution. Layered double hydroxides (LDHs) are two-dimensional materials with high CO₂ adsorption capacity and compositional flexibility with potential catalytic properties to be applied in CO₂ reduction processes. Herein, Zn-Cr LDH-based materials with different metal ratio and interlayer anions, i.e., chloride (Cl⁻), graphene quantum dots (GQDs), sodium dodecyl sulfate (SDS) and sodium deoxycholate (SDC), have been prepared by a co-precipitation method and characterized by different techniques. The influence of the interlayer inorganic and organic anions and the metal ratio on the application of Zn-Cr LDHs as catalysts for the photocatalytic CO₂ reduction reaction under visible light irradiation is unprecedentedly reported. The catalytic tests have been carried out with Ru(bpy)₃²⁺ as photosensitizer (PS) and triethanolamine as sacrificial electron donor (ED) at λ = 450 nm. All LDHs materials exhibited good photocatalytic activity towards CO. Among them, LDH3-SDC showed the best catalytic performance, achieving 10,977 μmol CO g⁻¹ at 24 h under visible light irradiation with a CO selectivity of 88%. This study provides pertinent findings about the modified physicochemical features of Zn-Cr LDHs, such as particle size, surface area and the nature of the interlayer anion, and how they influence the catalytic activity in CO₂ photoreduction.

Keywords: Zn-Cr layered double hydroxides; metal ratio; interlayer anion; photocatalysis; CO₂ photoreduction; CO selectivity



Citation: Gil-Gavilán, D.G.; Cosano, D.; Amaro-Gahete, J.; Castillo-Rodríguez, M.; Esquivel, D.; Ruiz, J.R.; Romero-Salguero, F.J. Zn-Cr Layered Double Hydroxides for Photocatalytic Transformation of CO₂ under Visible Light Irradiation: The Effect of the Metal Ratio and Interlayer Anion. *Catalysts* **2023**, *13*, 1364. <https://doi.org/10.3390/catal13101364>

Academic Editors: Adrián Pastor Espejo and Luis Sánchez Granados

Received: 14 September 2023

Revised: 6 October 2023

Accepted: 9 October 2023

Published: 12 October 2023



Copyright: © 2023 by the authors. Licensee MDPI, Basel, Switzerland. This article is an open access article distributed under the terms and conditions of the Creative Commons Attribution (CC BY) license (<https://creativecommons.org/licenses/by/4.0/>).

1. Introduction

In recent years, numerous efforts have been made to mitigate global warming and air pollution originating from the increase in carbon dioxide levels, as well as to solve the crucial social problem of dependence on non-renewable energy sources [1–4]. Among other detrimental factors, global climate change is largely caused by the increase in atmospheric CO₂ emissions originating from the burning of fossil fuels for energy production, deforestation, and industrial processes. Therefore, the photoreduction of CO₂ (CO₂PR) in high-added-value products has emerged as an environmental alternative to mitigate the greenhouse effect and energy problems through CO₂ capture and air purification [5–7]. Inspired by natural photosynthesis [8], the scientific community has developed many biomimetic approaches to design photocatalytic systems capable of converting CO₂

molecules into valuable fuels (CO, HCHO, HCOOH, CH₃OH and CH₄) under visible light irradiation [9,10]. Similarly to natural photosynthesis, CO₂PR processing artificial photosynthesis systems (APSs) are initiated with visible light absorption by a light-harvesting molecule or photosensitizer causing charge carrier generation. Subsequently, the photoinduced energy transfer assisted by the electron and hole charge separation promotes the well-known photo-redox artificial photosynthetic reaction based on the CO₂ reduction of chemical fuels as valuable C1 products and H₂O oxidation to molecular O₂. Regarding CO₂PR half-reaction, different catalysts have been used in these systems to increase the efficiency and selectivity of the process toward carbon-based chemical energy carriers [11,12], achieving good selectivity, as seen in other catalyzed CO₂-based chemical transformations [13]. Moreover, reaching high selectivity to CO is considered very promising from an industrial perspective, because it can serve as a valuable feedstock for the production of high-value-added products. This platform molecule is part of the so-called synthesis gas (syngas) composed of CO and H₂, which is a gas fuel with a rich chemical reactivity [14,15]. Syngas has potential applications, including: (i) the obtention of long-chain hydrocarbons (diesel–kerosene, gasoline, naptha. . .) used as synthetic fuels by the Fischer–Tropsch synthesis (FTS) process [16], (ii) methanol synthesis at high temperature (250–300 °C) and pressure (50–150 bar) [17], and (iii) hydrogen production by the water–gas shift reaction (WGSR) [18], among others.

In this current scenario, several materials have been studied as photocatalysts in photosynthesis-mimicking systems, providing important advantages such as visible light absorption, high mobility of photogenerated charge carriers, strong reduction capacity in CO₂PR and large surface area [19]. Layered double hydroxides (LDHs) are anionic clay materials with layered structure [6,20], also denoted “hydrotalcites,” that have attracted much attention as promising candidates for catalytic CO₂ conversion. LDHs present the general formula $[M^{II}_{1-x}M^{III}_x(OH)_2][A^{n-}]_{x/n} \cdot mH_2O$, where M^{II} is the divalent cation and M^{III} the trivalent one (i.e., Zn²⁺, Co²⁺, Mg²⁺, Cr³⁺, Al³⁺, Fe³⁺), Aⁿ⁻ represents the interlayer anion (i.e., Cl⁻, CO₃²⁻, NO₃⁻) and *x* indicates the molar metal ratio, which is variable between 0.17 and 0.33 [21], obtained from M^{III}/(M^{III} + M^{II}) ratio (Figure 1A). The structure of LDHs is based on brucite-like layers with positive charge counterbalanced with interlayered anions [3,6,22,23]. Compositional flexibility of LDHs enables their use in different prominent applications, such as photocatalytic [24] and electrocatalytic [25] CO₂ reduction, CO₂ capture for environmental remediation [26], photocatalytic hydrogen production [27], pollutant degradation [28], lithium–sulfur batteries [29], and adsorbents of atmospheric pollutants (CO₂, NO_x, SO_x and volatile organic compounds (VOCs)) [30], among others. The outstanding characteristics of LDHs, including their layered and tunable structure, their high thermal and chemical stability, their easy and inexpensive synthetic procedures, their optical features, their anion-exchange capacity and their high CO₂ adsorption capacity, make them exceptional materials for CO₂PR [6,31]. However, LDHs present inherent shortcomings, such as low specific surface area and deficient charge transfer [31], as well as poor visible light absorption [6], which makes difficult the achievement of enhanced photocatalytic performance. Therefore, the tris(2,2'-bipyridine)ruthenium(II) complex (Ru(bpy)₃²⁺) has been commonly used as photosensitizer (PS) in photocatalytic tests due to its broad absorption band in the visible light range ($\lambda_{max} = 450$ nm) and a relatively long lifetime of its excited state [32–35]. In addition, it is common to use triethanolamine (TEOA) or other compounds as a sacrificial electron donor (ED) because it restores the natural state of the PS [36]. The general mechanistic pathway for CO₂PR using LDHs as catalyst is illustrated in Figure 1B. Under visible light, the PS is excited and promotes an electron from HOMO to LUMO orbitals. Following an oxidative quenching route, the photogenerated electron is transferred to the LDH-based catalyst, and subsequently CO₂ is reduced to value-added products using the protons from water. Finally, the PS is regenerated when the sacrificial agent is oxidized [33].

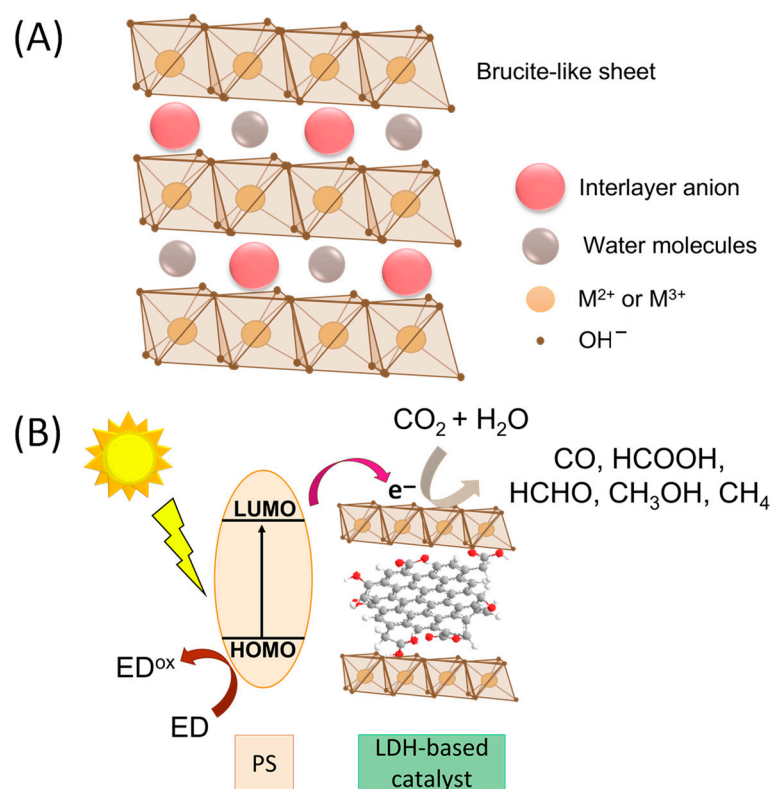


Figure 1. (A) LDH general structure. (B) General mechanism for visible light-driven CO₂PR using an LDH-based material as catalyst. ED: sacrificial electron donor. PS: photosensitizer.

The length and nature of the interlayer anion is considered one of the most relevant modulable LDH factors owing to the effect produced into the layered structure, chemical properties, and catalytic performance [28,37]. Anionic compounds intercalated between LDH sheets can be easily adjusted when different metal salt precursors are used or diverse anion exchange strategies are applied [28]. A fundamental parameter to study is the use of different interlayer anions giving rise to a wide variety of interlayer spaces, which is essential to obtain higher values of basal space for improvement in CO₂ adsorption [31] and the accessibility to the catalytic active sites in photocatalytic reaction systems. Concerning previous investigations, Iguchi et al. evaluated Ni–Al LDHs as catalyst in CO₂ photoreduction under UV irradiation and showed an improvement in CO selectivity with respect to H₂ production, which is the main competitive process. The conclusion from this work was the hole scavenger behavior of Cl[−] interlayer species in CO₂ photoreduction [10,38]. The electron–hole recombination was reduced due to the interaction of Cl[−] with photogenerated holes (h⁺) following these reactions [19]:



On the other side, carbonate ions inserted in the interlayer space can increase the performance in CO₂PR, because interlayer water molecules react with CO₂, generating H⁺, which are necessary for this reaction [39]. According to the literature, LDHs with CO₃^{2−} present higher CO₂ adsorption capacity than LDHs with Cl[−] [40] since carbonate ion confers higher LDH surface area than Cl[−], NO₃[−] and SO₄^{2−} [41]. Besides these advantages, it also acts as hole scavenger for the hydrogen evolution reaction (HER) [42]. According to Ng et al. [19], CO₃^{2−} was regenerated, being available for reacting with

photogenerated holes, which resulted in the formation of HCO_3^- or CO_3^{2-} . Moreover, hydroxyl groups were consumed and the reverse reaction for water splitting was unlikely. As a result, HER efficiency was improved [43], thus compromising the CO selectivity in CO_2 PR. Considering this disadvantage, carbonate ion is not the best interlaminar anion when using LDHs as catalysts for CO_2 PR. In the same way, Flores-Flores et al. stated that the photocatalytic performance of LDH-based materials can worsen when NO_3^- ions occupy the active sites because this makes CO_2 adsorption difficult [44]. Thereby, N-doped GQD/Co-Al LDH/g- C_3N_4 was synthesized by a hydrothermal treatment with urea and tested as catalyst in CO_2 PR under visible light, achieving an excellent CH_4 selectivity (99%). LDHs and g- C_3N_4 acted as light-harvesting semiconductors, while GQDs also worked as light-absorbing molecule and as electron mediator and storage [45].

Furthermore, cationic metals and metal ratio are crucial structural factors, which could affect crystallinity, light absorption, stability and reaction selectivity. The simple tunability of these parameters by changing the precursor metal salts and the proportion of divalent and trivalent cations can lead to the obtention of unique chemical properties and layer charge density in the resulting LDH materials [37]. Likewise, both factors are related to bandgap energy and CO_2 adsorption, which is based on the basicity of the metal incorporated into the LDH structure. The CO_2 adsorption capacity of an LDH will be higher as the basicity of the metallic cations increases. It is well known that LDHs composed of Mg^{2+} or Zn^{2+} as divalent cations show optimal CO_2 adsorption [31,46]. Hong et al. investigated different LDHs and g- C_3N_4 and concluded that Mg-Al LDHs had higher CO_2 adsorption capacity [47]. The metal ratio also influences the thermal stability of Mg-Al LDHs, which increases at a lower metal ratio [48]. Mg-Zn-Al LDHs with different metal ratios were synthesized by Sakr and coworkers, who evaluated the influence of Zn^{2+} metal concentration on properties such as the particle size. The higher the Zn^{2+} amount, the lower the particle size was. Thus, the particle size was approximately 20 nm when the Mg:Zn molar ratio was 1:3 [49]. Moreover, this material presented the highest CO_2 adsorption capacity, which could be attributed to its optimal textural properties. Alternatively, Ni-Al LDHs with different metal ratios were synthesized for CO_2 PR applications. The highest CH_4 selectivity was obtained using the Ni-Al LDHs with metal ratio 2 as catalyst [50]. In a subsequent study, Co-Al LDHs with different Pd amounts were synthesized and applied for CO_2 photoreduction to produce syngas from water. The LDHs catalysts did not show any selectivity towards CO evolution, although it was possible to control the CO/ H_2 ratio depending on the Pd amount [51]. Zn-Cr LDHs have attracted particular interest for photocatalytic applications due to two primary reasons: (i) the high catalytic activity provided by their metal cations, and (ii) its capacity to absorb light in the visible region [43,46]. Indeed, Zn-Cr LDH-based materials with different metal ratios (2:1, 3:1, 4:1) were obtained by a co-precipitation method and applied as catalysts in photocatalytic hydrogen production [43]. The study revealed that the crystallinity and the hydrogen evolution were higher when the material presented lower metal ratio. Concerning CO_2 PR, Zn-Cr LDH/ Cu_2O have been evaluated as catalysts for CO_2 reduction to CO under UV irradiation. Zn-Cr LDHs acted as light-harvesting material whereas Cu_2O provided the catalytically active sites for the photocatalytic reaction [52]. Additionally, Pd(Zn-Cr LDH/g- C_3N_4) was synthesized by a hydrothermal treatment and tested as catalyst in CO_2 PR under visible light, achieving high reduction efficiency to CH_4 [47].

Graphene is a promising material to form composites due to its excellent mechanical, optical and electronic properties [53] such as conductivity and flexibility [54]. Specifically, GQDs are a zero-dimensional graphene-based material with exceptional properties, such as highly tunable photoluminescence and photostability properties in addition to those of graphene [55]. Moreover, GQDs could be used for enlarging interlaminar space in the same way as SDS and SDC. The formation of composites allows us to enhance the thermal and catalytic stability [56] and improve textural properties with respect to bulk materials, thus enhancing CO_2 adsorption [57], and could augment the photocatalytic performance, since the resulting composites would have the advantages of both starting materials [58].

Herein, the synthesis of several Zn-Cr LDH materials with different interlayer anions, i.e., chloride ion (Cl^-), graphene quantum dots (GQDs), sodium dodecyl sulfate (SDS) and sodium deoxycholate (SDC), and distinct metal ratios is described. The prepared materials have been characterized by different instrumental techniques and evaluated as catalytic units of a three-component photocatalytic system for CO_2 reduction under visible light ($\lambda = 450 \text{ nm}$).

2. Results and Discussion

Zn-Cr LDHs with different interlayer anions and metal ratios have been prepared by a conventional co-precipitation method at 60°C and $\text{pH} = 9.5$ [59]. The nomenclature used for these materials was LDHX-A, where X was the Zn/Cr metal ratio and A was the incorporated interlayer anion. Zn and Cr contents in mmol/g and metal ratio values were obtained by ICP-MS (Table 1). The experimental Zn/Cr ratios (X) of LDHX-A materials were very close to the theoretical ones. Elemental analysis measurement revealed a carbon content in LDH3-GQD of 6.3% C, mostly originating from GQDs.

Table 1. Zn and Cr compositions and Zn/Cr metal ratio measured by ICP-MS.

Sample	Zn (mmol/g)	Cr (mmol/g)	Zn/Cr Molar Ratio
LDH2-Cl	5.11	2.42	2.1
LDH3-Cl	5.88	1.78	3.3
LDH4-Cl	6.26	1.51	4.1
LDH3-GQD	5.64	1.68	3.3
LDH3-SDS	4.19	1.20	3.5
LDH3-SDC	2.64	0.91	3.5

The structural study of the synthesized LDHX-A was carried out by X-ray diffraction (XRD). XRD patterns of LDH-based materials showed the characteristic diffraction peaks at 11.4° , 22.9° , 33.6° and 59.7° , which corresponded to 003, 006, 009 and 110 diffraction planes, respectively, typical from R-3m symmetry (Figure 2) [60]. When the interlayer distance increased due to the intercalation of organic anions, the main diffraction peaks appeared at lower angle values [5]. Then, the bands attributed to the 003 diffraction plane were located at 7.3° , 3.5° and 2.6° , for LDH3-GQD, LDH3-SDS and LDH3-SDC, respectively. The crystallite size (D , nm), basal space (d_{003} -value, nm), cation–cation distance in the brucite-like layer (a , nm) and the variable related to three times the distance between adjacent brucite-like layers (c , nm) were parameters calculated and reported in Table 2. The value d_{003} in LDHs with chloride as interlayer anion was 0.79 nm [61,62], whereas for GQDs, SDS and SDC, it was 1.21 nm [63], 2.60 nm [64] and 3.27 nm [65], respectively (Figure 3). Likewise, the c parameter shifted to higher values in LDH3-GQD, LDH3-SDS and LDH3-SDC with respect to LDH3-Cl. Thus, the data obtained for Cl^- , GQDs, SDS and SDC were 2.34 nm [66], 3.65 nm, 7.74 nm [64] and 10.00 nm [59], respectively. The a parameter between metal cations was similar in all samples due to the similar layer composition in terms of metal identity. Moreover, an increase in the crystallite size D calculated using Scherrer equation was observed with further expansion of the interlayer space. The presence of zinc oxide (ZnO) was revealed in LDH3-Cl, LDH3-GQD, LDH3-SDS and LDH4-Cl by the appearance of its three characteristic bands in the range of 30° to 38° . The formation of this oxide is quite common in the synthesis of Zn-based LDHs [67]. In this sense, Tichit et al. determined that the amount of ZnO could be reduced at lower temperatures of LDH synthesis [68], which could be interesting for future synthesis processes and investigations.

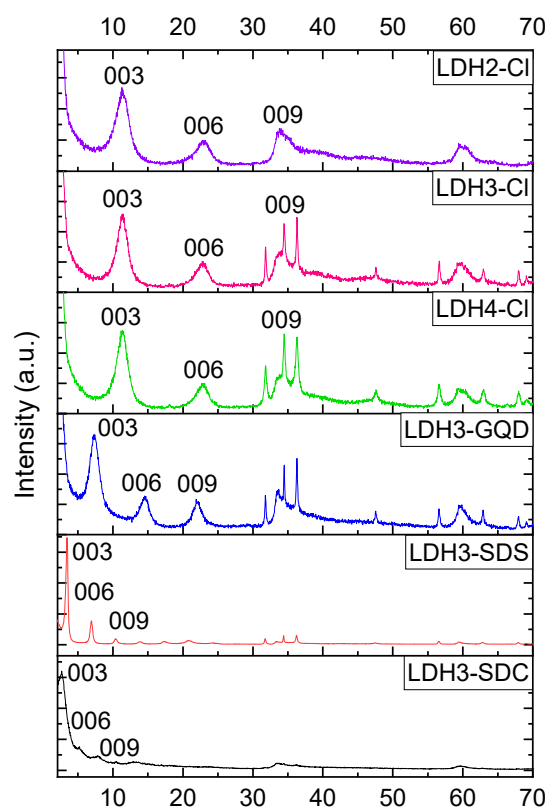


Figure 2. XRD patterns of the synthesized materials.

Table 2. Lattice parameter and crystallite size of synthesized materials.

Sample	d_{003} (nm) ^a	c (nm) ^a	a (nm) ^a	D (nm) ^b
LDH2-Cl	0.79	2.35	0.31	3.352
LDH3-Cl	0.78	2.34	0.31	4.157
LDH4-Cl	0.78	2.33	0.31	3.960
LDH3-GQD	1.21	3.65	0.31	5.417
LDH3-SDS	2.60	7.74	0.31	20.758
LDH3-SDC	3.27	10.00	0.31	41.497

^a Lattice parameter; ^b crystallite size.

Raman spectroscopy was accomplished to identify the stretching vibration of the LDHX-A. Raman spectra displayed in Figure 4a showed the presence of metal–oxygen bonds and interlaminal anions from the LDH structure. The typical hydroxyl stretching bands and M–O symmetric vibrations of LDH compounds at 3570–3629 cm^{-1} and 513–538 cm^{-1} , respectively, were observed in all materials [69,70]. LDH3-GQD exhibited typical 1417 cm^{-1} (D band) and 1617 cm^{-1} (G band) signals attributed to sp^3 and sp^2 carbon domains in graphene-based materials, respectively [71]. In the case of LDHs prepared with intercalated SDS, the peaks associated with CH_3 symmetric stretching and CH_2 symmetric stretching vibrations appeared at 2882 cm^{-1} and 2851 cm^{-1} , respectively. In addition, S=O asymmetric and S=O symmetric stretching bands were identified at 1297 cm^{-1} and 1064 cm^{-1} , respectively [72]. Regarding SDC-based compounds, the peaks observed at 2937 cm^{-1} and 2869 cm^{-1} were associated with CH_3 and CH_2 vibrational modes from the SDC hydrocarbon chain. The bands at 1439–1453 cm^{-1} in LDH3-SDS and LDH3-SDC were related to CH_3 asymmetric bending [59].

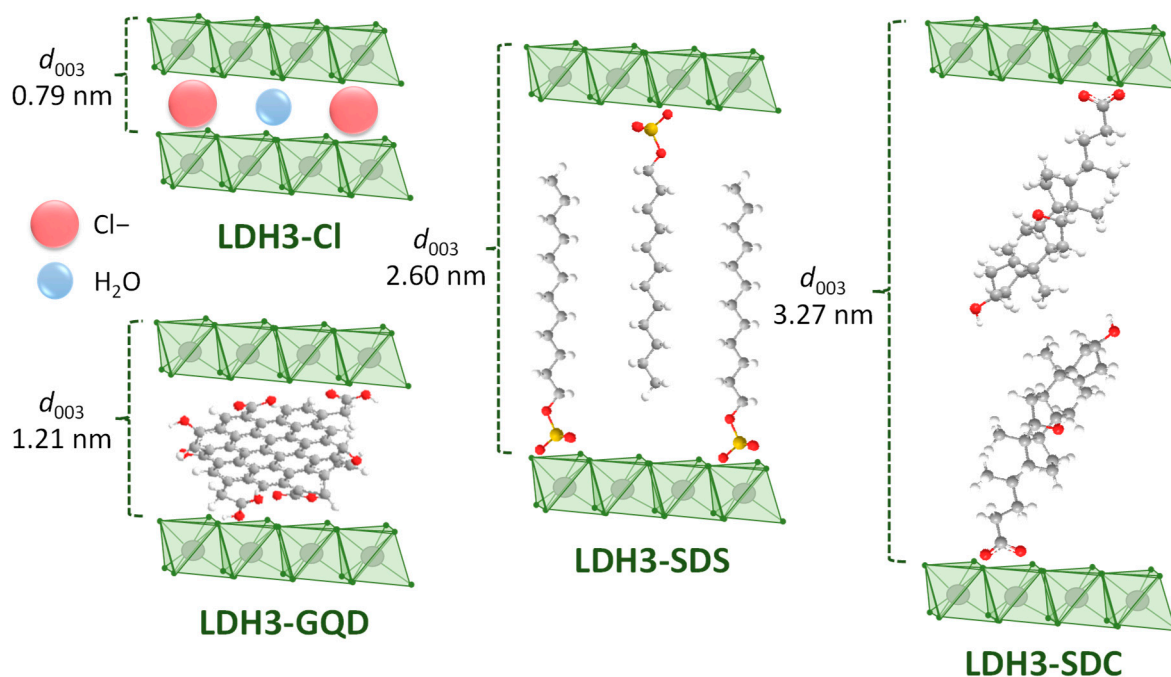


Figure 3. Schematic illustrations of different interlayer anion arrangement in Zn-Cr LDHs.

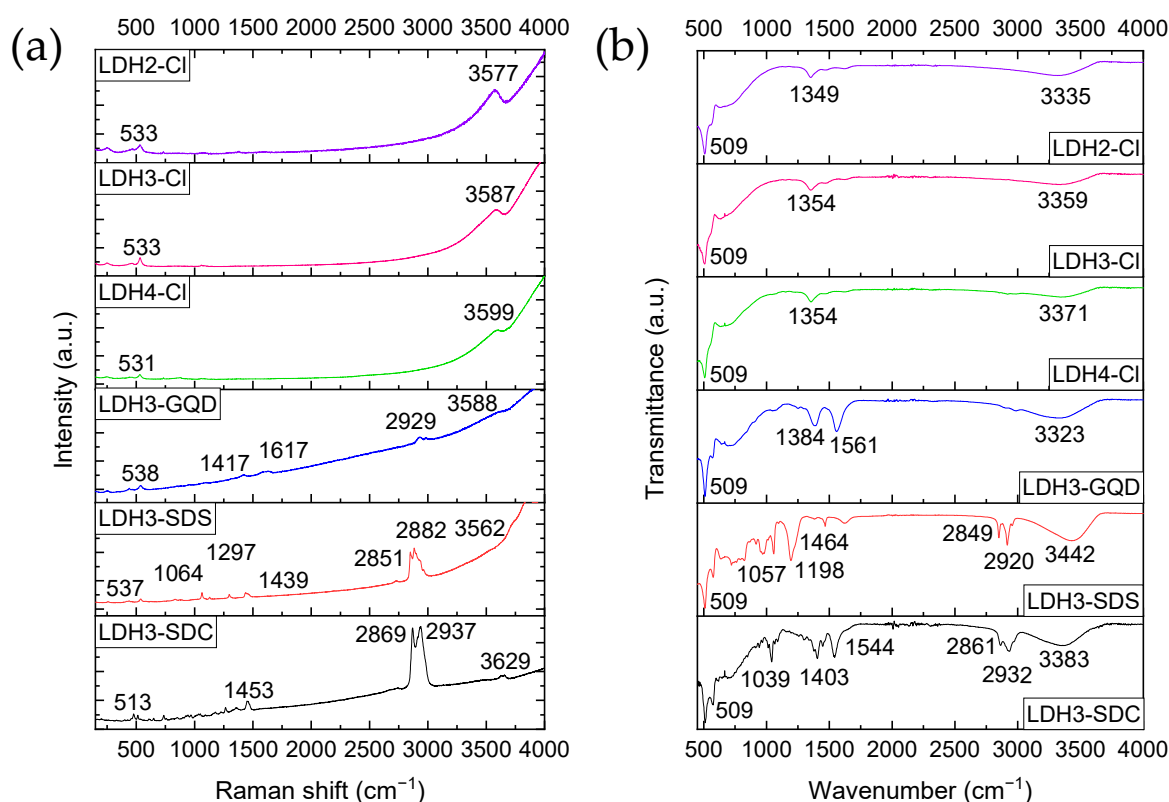


Figure 4. (a) Raman and (b) FTIR-ATR spectra of synthesized LDHs.

Fourier-transform infrared spectroscopy with attenuated total reflectance (FTIR-ATR) was performed to complement the results obtained by Raman spectroscopy. FTIR-ATR spectra of synthesized LDHX-A illustrated in Figure 4b corroborated the LDH structure and the presence of GQDs, SDS and SDC interlayer anions. All materials presented a broad band between 3323 cm^{-1} and 3442 cm^{-1} attributed to OH stretching vibration and a narrow peak at 509 cm^{-1} ascribed to M-O lattice vibrations [73]. FTIR-ATR spectra of LDHX-Cl

showed a pronounced peak at $1349\text{--}1354\text{ cm}^{-1}$ that was attributed to carbonate ion [60,74]. Although the precursor used for the synthesis of these materials was a chloride salt, carbonate ions from the atmosphere were also incorporated as interlayer anions in the LDH structure. In contrast, LDH3-GQD spectra exhibited the two characteristic bands of GQDs at 1384 cm^{-1} and 1561 cm^{-1} , which were associated with C–O bond stretching and C=C stretching vibrations from skeletal polycyclic aromatic hydrocarbons, respectively [75,76]. Conversely, infrared spectra obtained for LDH3-SDS displayed the typical peaks ascribed to C–H stretching vibrations, appearing at 2849 cm^{-1} and 2920 cm^{-1} . The band at 1464 cm^{-1} was related to CH_2 bending vibrations. Furthermore, the characteristic antisymmetric and symmetric stretching vibrations of S=O of SDS interlayer anion presented at 1057 cm^{-1} and 1198 cm^{-1} , respectively [77]. Analogously to the LDH3-SDS, C–H vibration modes were also revealed for the LDH3-SDC at 2861 cm^{-1} and 2932 cm^{-1} . In addition, the symmetric and asymmetric stretching vibrations of carboxyl group were observed at 1544 cm^{-1} and 1403 cm^{-1} , respectively. Lastly, C–H plane bending vibrations also appeared at 1039 cm^{-1} [65].

The microstructure and morphology of the samples have been analyzed by transmission electron microscopy (TEM). Compositional analysis has been also performed by chemical mapping using energy-dispersive X-ray spectroscopy combined with scanning transmission electron microscopy (STEM-EDS). The morphology of the LDH3-Cl sample is illustrated in Figure 5a and was comprised of numerous nanosheets with an irregular shape and very wide size distribution, from few dozen to several hundred nanometers. In addition, these nanosheets were interconnected, forming agglomerated structures. The bottom-right inset of Figure 5a shows an HRTEM image of one nanosheet and the corresponding FFT pattern. It can be observed that the nanolayer was nicely orientated along the $\langle 01\text{-}11 \rangle$ zone axis and the analysis provided interplanar distances of 0.14 nm, 0.19 nm and 0.25 nm ascribed to (110), (112) and (102) planes, respectively. These values were consistent with those reported in the literature [78,79]. Selected area electron diffraction (SAED) pattern involving many of these nanosheets, shown at the bottom-left inset Figure 5a. Coherently, it corroborated the diffraction rings related to these planes.

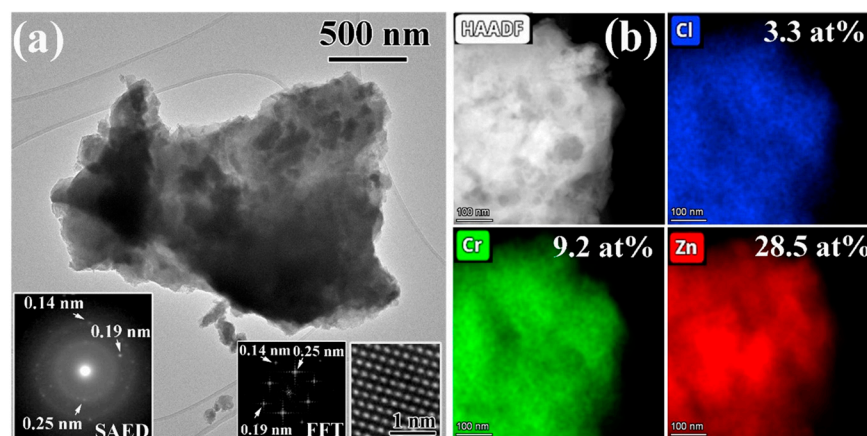


Figure 5. (a) TEM images of LDH3-Cl. SAED pattern and HRTEM (with its corresponding FFT) are also included. (b) EDS elemental mapping of LDH3-Cl.

Lattice parameters a and c can be calculated using the relationship between interplanar distance d_{hkl} and Miller index for a hexagonal structure [80]:

$$\left(\frac{1}{d_{hkl}}\right)^2 = \frac{4}{3} \left(\frac{h^2 + hk + k^2}{a^2}\right) + \frac{l^2}{c^2} \quad (4)$$

Thus, using $d_{110} = 0.14\text{ nm}$ and $d_{102} = 0.25\text{ nm}$ in Equation (4) we obtain $a = 0.30\text{ nm}$ and $c = 0.58\text{ nm}$. Since the LDH structure comprises five planes, i.e., four interplanar distances,

then the LDH structure height c_h should be calculated as $c_h = 0.58 \text{ nm} \times 4 = 2.32 \text{ nm}$. These values are in good agreement with results obtained by XRD (vide supra). EDS elemental mapping of LDH3-Cl is shown in Figure 5b. Quantification results are also indicated. It is worth emphasizing that the Zn:Cr ratio was very close to the at% nominal 3:1 ratio. This sample used Cl^- as interlaminar anion, and the Cl elemental map clearly showed that it was fully embedded throughout the whole structure.

LDH2-Cl microstructure is shown in Figure S1a. The morphology and structure were similar to the LDH3-Cl sample. SAED pattern provided same interplanar distance values. Lattice parameter a and c remained unaltered, as also confirmed by XRD measurements (see Table 2). EDS quantification (Figure S1b) also confirmed the at% nominal 2:1 ratio for Zn:Cr elements.

Repeatedly, similar TEM results were found for LDH4-Cl sample (Figure S2a). No changes in the lattice parameter a and c were observed by increasing the Zn:Cr ratio to 4:1. EDS corroborated this at% nominal ratio. In this sample, Cl^- was also operating as interlaminar anion. Unfortunately, in this sample, EDS mapping had to be performed in other areas (Figure S2b) due to some instabilities that finally led to the fall of our TEM-investigated agglomerate.

Figure 6a corresponds to the TEM analysis for LDH3-GQD sample. The SAED pattern exhibited diffraction rings ascribed to (110) and (102) planes, providing interplanar distances of about 0.14 nm and 0.29 nm, respectively, so (110) interplanar distance remained unchanged, and consequently, lattice parameter a preserved its value, as inferred from Equation (1) and also confirmed the XRD measurements (see Table 2). However, it seems that the presence of GQDs increased the (102) interplanar distance to 0.29 nm, leading to a an LDH structure height c_h value close to 3.00 nm. This increase was also observed by XRD providing a slightly higher value. Besides LDH diffraction rings, the SAED pattern also showed a dotted diffraction ring coming from GQD (100) planes with an interplanar distance of 0.21 nm in agreement with previously reported studies [81]. EDS elemental mapping is shown in Figure 6b. In this sample, GQDs were acting as interlaminar anions. Their elemental mapping revealed that GQDs were well distributed throughout the sample. In addition, the Zn:Cr ratio was very close to the at% nominal 3:1 ratio.

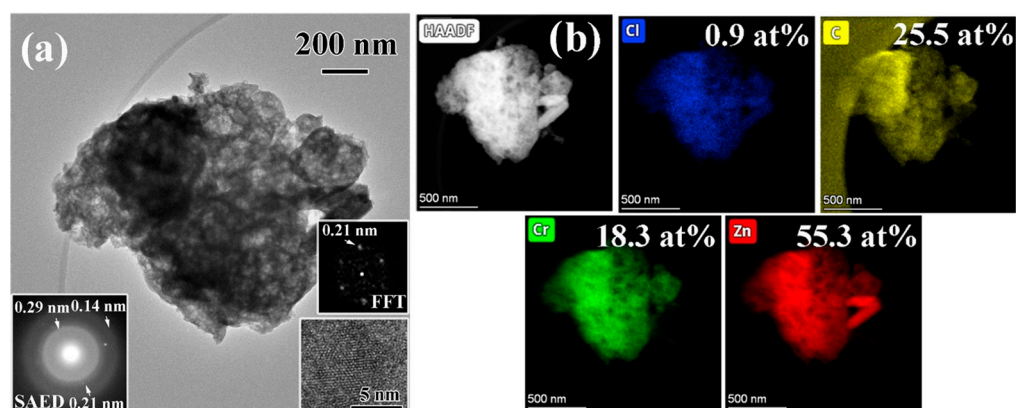


Figure 6. (a) TEM images of LDH3-GQD including a SAED pattern and HRTEM imaging (with its corresponding FFT). (b) EDS elemental mapping of LDH3-GQD.

Regarding TEM study for LDH3-SDS (Figure 7a) and LDH3-SDC (Figure 8a), a similar lattice distortion was discerned. In both samples, the lattice parameter a remained unaltered, since (110) interplanar distance was again 0.14 nm. However, (102) interplanar distance, which was 0.25 nm for the LDH3-Cl sample, was now increased to an average value of about 0.29 nm. It is important to point out that (102) diffraction ring became like a broad ring, making it difficult to obtain an accurate value for lattice parameter c . Moreover, some fringes in both LDH3-SDS and LDH3-SDC at higher magnification were observed, being more separated in the later. This dark contrast in conventional TEM imaging could come from Zn and Cr

elements, which have higher Z atomic number, and consequently from LDH layers. These images are incorporated as insets in Figures 7 and 8. It was hard to make an estimation of LDH structure height c_h since probably basal plane was not oriented perpendicularly to the electron beam and then measurements would be underestimated. However, distance between fringes was at least about 5 nm for LDH3-SDS and almost 10 nm for LDH3-SDC, in agreement with XRD results. EDS quantification results provided an at% Zn:Cr ratio close to the nominal 3:1 for both LDH3-SDS and LDH3-SDC samples. Moreover, the S element was also present in the LDH3-SDS sample due to SDS interlamellar anion.

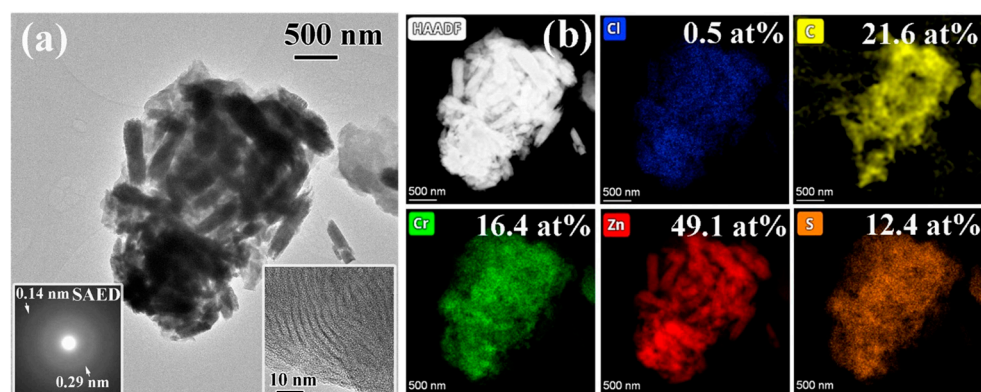


Figure 7. (a) TEM images of LDH3-SDS sample including an SAED pattern and HRTEM imaging. (b) EDS elemental mapping.

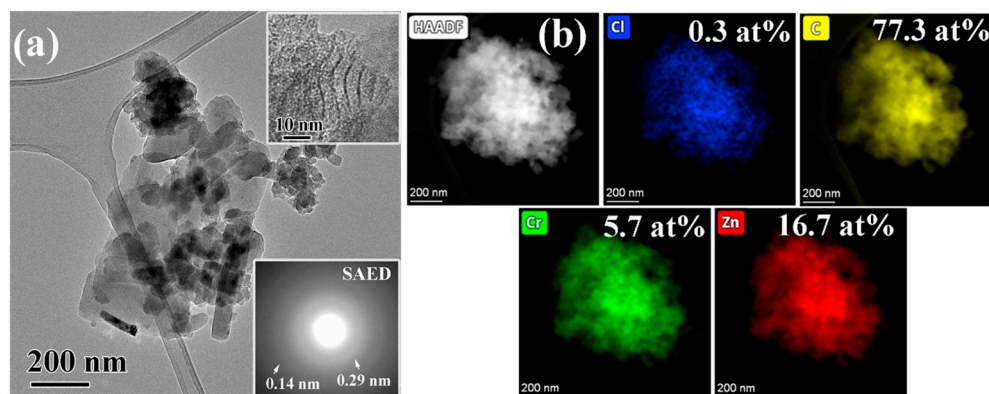


Figure 8. (a) TEM images of LDH3-SDC sample including an SAED pattern and HRTEM imaging. (b) EDS elemental mapping.

Particle size distribution curves of LDHX-A samples are displayed in Figure S3. As shown, the materials with lower particle sizes were LDH3-Cl, LDH4-Cl and LDH3-SDC with the most abundant particle sizes being approximately 29 μm , 20 μm and 46 μm , respectively. On the other hand, LDH3-SDS showed higher particle sizes, with a maximum centered at 212 μm . Larger particles promote less dispersibility of the materials and greater light scattering in solution [82], thus negatively affecting photocatalytic activity. Therefore, smaller particles in which more active sites are exposed would be desirable [83] in order to affect the light scattering to a lesser extent during photocatalytic reaction.

The textural properties of synthesized materials were examined by analysis of the nitrogen adsorption–desorption isotherms. BET surface area, pore diameter and pore volume values for LDHX-A samples are given in Table 3. Nitrogen isotherms and pore size distributions for the synthesized materials are shown in Figure 9. Most LDHs had rather low specific surface area, particularly LDH2-Cl, LDH3-Cl and LDH3-SDS, and displayed type II isotherms, typical of non-porous materials [84]. LDH3-GQD exhibited type IV isotherm [73,85] with very large pores and the largest surface area. LDH4-Cl and LDH3-

SDC presented moderate surface areas. All of them showed a wide distribution of pore sizes.

Table 3. Textural properties of the LDHX-A materials.

Sample	S_{BET} (m ² /g)	Pore Diameter (nm)	Pore Volume (cm ³ /g)
LDH2-Cl	1	3.9	0.003
LDH3-Cl	5	4.0	0.005
LDH4-Cl	54	4.4	0.059
LDH3-GQD	111	12.2	0.340
LDH3-SDS	4	8.9	0.008
LDH3-SDC	42	11.4	0.121

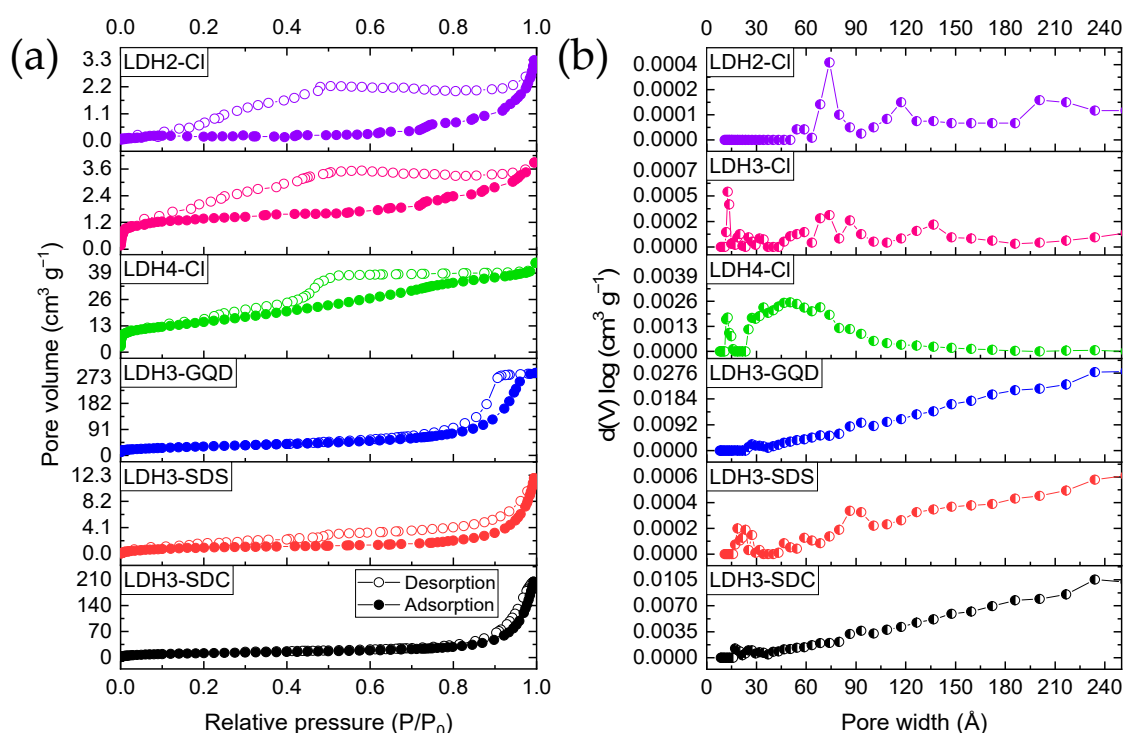


Figure 9. (a) Nitrogen adsorption–desorption isotherms and (b) pore size distributions determined by a DFT method of LDHX-A materials.

The UV-vis diffuse reflectance spectra of LDHX-A are represented in Figure S4a. The absorption bands at 410 nm and 560 nm arose from Cr³⁺ d-d transitions $^4A_{2g}$ $^4T_{2g}(F)$ and $^4A_{2g}$ $^4T_{1g}(F)$ [61,74,86]. The bandgap of each material has been calculated using the Kubelka–Munk function from the plots of $(F(R)h\nu)^2$ vs. $h\nu$ (Figure S4b) [27] and was in concordance with those values previously reported for Zn-Cr LDH-based materials [19]. Thus, bandgaps between 2.62 and 2.79 eV were obtained with LDHs, with intercalated GQDs, SDS and SDC having a slight shift to higher values.

Photocatalytic reactions revealed that all synthesized LDHX-A materials were active in the CO₂ photoreduction to CO under visible light ($\lambda = 450$ nm) (Figure 10) using Ru(bpy)₃²⁺ and TEOA as photosensitizer and sacrificial electron donor, respectively. Firstly, photocatalytic tests of Zn-Cr LDHs samples with different metal ratio and chloride ion as interlayer anion were performed (Figure 10a). The light-driven CO production was 7620 $\mu\text{mol CO g}^{-1}$ at 24 h using LDH4-Cl as catalyst, followed by LDH3-Cl and LDH2-Cl with 7052 $\mu\text{mol CO g}^{-1}$ and 4922 $\mu\text{mol CO g}^{-1}$, respectively. Noteworthy, LDHs with a lower amount of Cr³⁺ resulted in a higher catalytic activity. However, LDHX-Cl with metal ratio 3 showed

the highest CO selectivity (Figure 10c) and was chosen to study the influence of different interlayer anions. Therefore, the ratio of metal cations in Zn-Cr LDH-based materials with chloride as interlayer anion affected the photocatalytic performance and selectivity toward CO evolution.

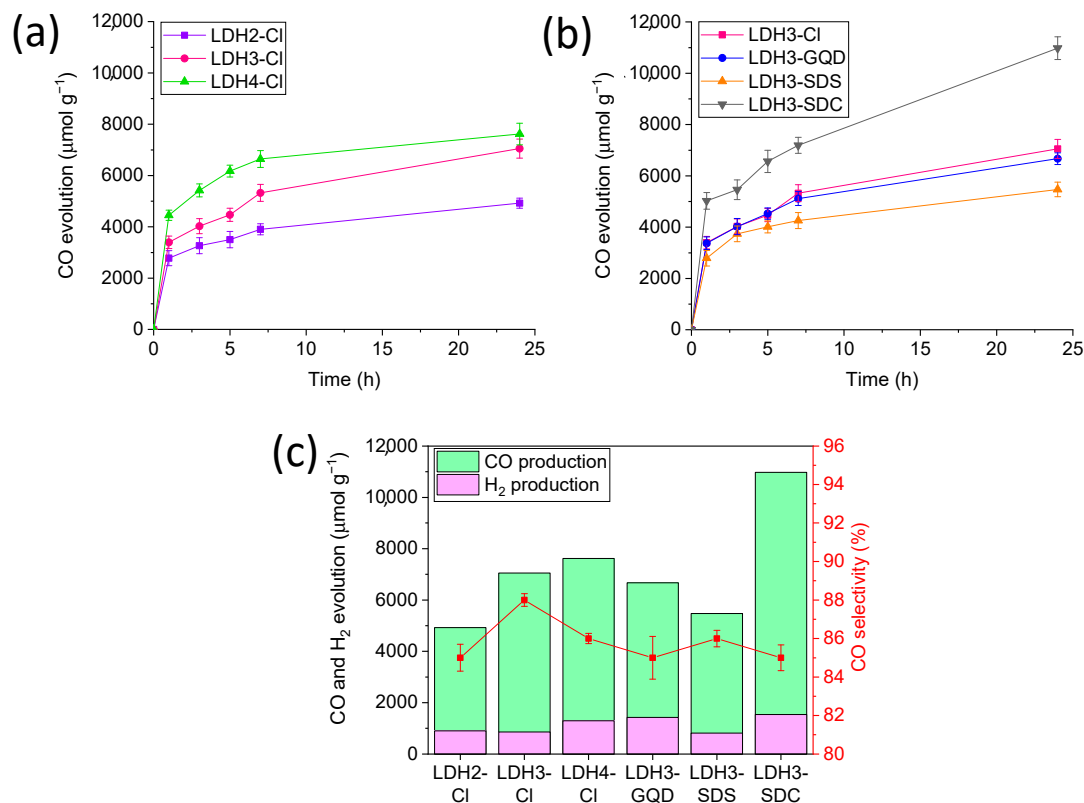


Figure 10. CO evolution for the photocatalytic systems: (a) using different metal ratio and chloride as interlayer anion, (b) using different interlayer anion and metal ratio of ca. 3 and (c) CO/H₂ evolution after 24 h of reaction and CO selectivity considering similar catalytic conversion.

Then, the photocatalytic performance of the Zn-Cr LDH-based compounds was evaluated using different interlaminar anions (Cl⁻, GQDs, SDS and SDC) while maintaining a metal ratio of 3 (Figure 10b). The photocatalytic activity at 24 h decreased in the following order: LDH3-SDC (10,977 μmol CO g⁻¹) > LDH3-Cl (7052 μmol CO g⁻¹) > LDH3-GQD (6671 μmol CO g⁻¹) > LDH3-SDS (5471 μmol CO g⁻¹). The highest catalytic activity was observed for LDH3-SDC, which had the largest basal spacing value, a moderate surface area and low particle size, which improved the catalyst dispersibility and the access to the active sites and minimize light-scattering effects. Although LDH3-Cl exhibited low surface area and interlaminar spacing, the material achieved outstanding catalytic performance. This enhanced catalytic behavior could be associated with the small particle size shown by this material and the role of chloride ion as hole scavenger during CO₂PR process [10]. It is worth noting that the presence of GQDs did not significantly improve the conversion and did not make the reaction possible without photosensitizer at 450 nm, despite leading to a significant increase in surface area, pore diameter and pore volume. In this sense, it is suggested that the active sites may be blocked and inaccessible to CO₂ molecules. Additionally, LDH3-GQD consisted of particle agglomerates with a wide size distribution observed and corroborated by TEM and particle size measurements, which could compromise the dispersibility and accessibility to the catalytic units. It could be thought that the ZnO present in samples LDH3-Cl, LDH3-GQD, LDH3-SDS and LDH4-Cl would be able to generate catalytic activity. Several authors have reported that ZnO catalyzes the CO₂ photoreduction [87,88]. For example, Wang, et al. synthesized a material based

on carbon co-doped ZnO that was tested as catalysts in a CO₂ photoreduction system using Ru(bpy)₃Cl₂ (2.23×10^{-3} M) as photosensitizer. The catalytic carbon co-doped ZnO material reached 1500 $\mu\text{mol CO g}^{-1}$, so it was capable of achieving certain activity [89]. In our photocatalytic system, ZnO was not the main material responsible for CO₂PR. Thus, LDH3-SDC presented excellent photocatalytic activity in the absence of ZnO, whereas LDH3-GQD and LDH3-SDS, which contained ZnO, gave lower values of photocatalytic CO evolution. Consequently, our studied photocatalytic CO₂ reduction system integrating Ru(bpy)₃Cl₂ at low concentration (4.41×10^{-4} M), 1 mg of LDHX-A material, mainly containing LDHs, and a minor contribution of ZnO (in LDH3-Cl, LDH3-GQD, LDH3-SDS and LDH4-Cl), evidenced a negligible contribution of ZnO in the resulting photocatalytic performance.

The photocatalytic results in HER are displayed in Figure S6, where H₂ production values between 860 and 1537 $\mu\text{mol g}^{-1}$ at 24 h can be observed. CO selectivity was calculated for each material in the proposed photocatalytic system at similar catalytic conversion (ca. 5000 $\mu\text{mol CO g}^{-1}$). The obtained values, as well as the CO/H₂ production at 24 h of reaction, are shown in Figure 10c. CO selectivity decreased in the sequence LDH3-Cl (88%) > LDH3-SDC (86%) = LDH3-SDS (86%) = LDH4-Cl (86%) > LDH2-Cl (85%) = LDH3-GQD (85%). Therefore, the synthesized materials achieved similar CO selectivity at analogous CO production. There were no significant changes in CO selectivity results at 24 h of reaction. These values were 90%, 88%, 86%, 86%, 85% and 84% for LDH3-Cl, LDH3-SDC, LDH3-SDS, LDH4-Cl, LDH2-Cl and LDH3-GQD, respectively. Figure S7a,b give CO selectivity at different times for the synthesized materials in the proposed photocatalytic system. In addition, syngas ratios were determined for each material during the photocatalytic reaction (Figure S7c,d). They were in concordance with the CO/H₂ ratios reported in the literature [90].

Values of apparent quantum yield (AQY) were calculated and are shown in Table S1. As expected, the obtained AQY corroborated the abovementioned results in photocatalytic performance. The photocatalytic system with LDH3-SDC exhibited an outstanding AQY (2.4%) compared to other CO₂ photoreduction systems using LDH-based materials as catalysts [33]. LDH3-SDC photocatalytic performance and CO selectivity were compared with other LDH materials reported in the literature when they acted as catalysts in CO₂ photoreduction systems under visible light using Ru(bpy)₃Cl₂ as PS and TEOA as ED (Table S2). Noteworthy, LDH3-SDC achieved excellent photocatalytic activity and exhibited the highest CO selectivity reported so far for these photocatalytic systems under similar experimental conditions using the same PS and ED components.

Control photocatalytic tests were carried out in the absence of photosensitizer, sacrificial electron donor and catalyst to elucidate the role of each component and the reaction mechanism. Without photosensitizer and sacrificial electron donor, CO evolution was not observed. The photosensitizer was required as light-harvesting unit due to the weak light-harvesting ability of LDHs in the visible region [27,32]. Although their bandgap values were included in the visible region, LDH-based materials did not act as semiconductors in our CO₂PR system. For its part, TEOA was indispensable because it provided the necessary electrons to regenerate Ru(bpy)₃²⁺ and continue the photocatalytic CO₂ reduction cycle. On the other hand, the control test without catalyst gave some activity towards CO due to the intrinsic photocatalytic activity of the ruthenium complex [91], resulting in 3.2 $\mu\text{mol CO}$ at 24 h of light irradiation. This activity was practically reached at 3 h of reaction, since Ru(bpy)₃²⁺ mainly degrades during the first 4 h under visible irradiation [92]. Despite the requirement of the ruthenium complex in the photocatalytic system to harvest light, Zn-Cr LDH-based material enabled the continuous CO production for up to 24 h, specifically reaching 11.0 $\mu\text{mol CO}$ (10,977 $\mu\text{mol CO g}^{-1}$) with LDH3-SDC. Consequently, these materials exhibited improved photocatalytic performance with respect to the PS. An additional control experiment was carried out under inert nitrogen atmosphere to corroborate that CO came from reduction of bubbled CO₂ and not from adsorbed CO₂ or residual carbonate

in the LDH interlayer. Our results demonstrated that there was no CO evolution when the photocatalytic system was bubbled with N₂.

According to the literature [93], the proposed mechanism is initiated with the visible light excitation of the photosensitizer component Ru(bpy)₃²⁺. Thus, an electron is promoted from HOMO to LUMO orbitals of these ruthenium species. Based on PL measurements, it is accepted that the ruthenium complex excited state, Ru(bpy)₃^{2+*}, is quenched by the Zn-Cr LDH-based catalysts [33], following an oxidative quenching pathway. Therefore, the excited photosensitizer is oxidized to Ru(bpy)₃³⁺ by transferring an electron to the catalytic entities. Subsequently, CO₂, with protons from water is catalytically reduced to CO by Zn-Cr LDH catalytic units. Finally, the oxidized sensitizer, Ru(bpy)₃³⁺ is regenerated to the initial ruthenium complex state, Ru(bpy)₃²⁺, by the sacrificial electron donor, TEOA, which is oxidized to TEOA⁺ [51] (Figure 11).

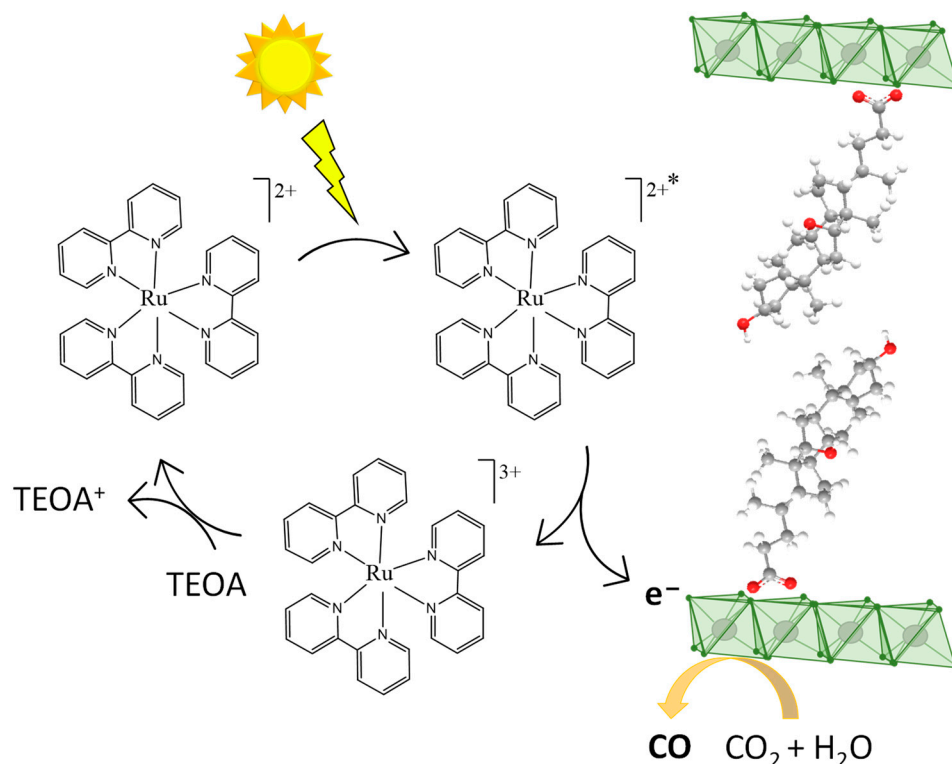


Figure 11. Schematic representation of the photocatalytic CO₂ reduction process. (*): PS excited state.

The stability of LDH3-SDC after 24 h of reaction was studied using different techniques. TEM images (Figure S8a) revealed that 24 h-irradiated LDH3-SDC also consisted of irregular and agglomerated sheets. The bottom-left inset of Figure S8a shows an HRTEM image of one nanolayer and the top-left inset the corresponding SAED pattern. It exhibited diffraction rings from (110) and (102) planes, providing interplanar distances of about 0.14 nm, 0.25 nm and 0.29 nm. It could be noted that 0.25 nm and 0.29 nm corresponded to the presence of CO₃²⁻/Cl⁻ and SDC as interlayer anions, respectively (vide supra). EDS elemental mapping (Figure S8b) corroborated a nominal at% Zn:Cr ratio of 3:1. Although the at% of C (from SDC) in 24 h-irradiated LDH3-SDC (58.3%) was lower than in pre-irradiated LDH3-SDC (77.3%), this material presented mainly SDC as interlayer anion and a minor contribution of CO₃²⁻/Cl⁻. FTIR-ATR spectra corroborated that LDH structure was preserved by the appearance of the bands at 3318 cm⁻¹ and 514 cm⁻¹, attributable to OH stretching and M-O lattice vibrations, respectively. In addition, the spectra displayed bands at 2943 cm⁻¹, 2873 cm⁻¹, 1435 cm⁻¹ and 1039 cm⁻¹ related to C-H and carboxyl group vibrations of SDC (Figure S8c). Considering the structural and morphological characterization, LDH3-SDC seemed to be photostable, but when it was used for three runs

only, it reached $7033 \mu\text{mol g}^{-1}$ after 72 h of irradiation (Figure S8d). The decrease in its catalytic performance cannot be ascribed to its photodegradation, but instead, it suggests the influence of other factors, such as SDC loss and poisoning, among others.

3. Materials and Methods

3.1. Reagents and Materials

Citric acid monohydrate (Labkem, Barcelona, Spain), sodium hydroxide (Labkem Barcelona, Spain), sodium dodecyl sulfate (Sigma Aldrich, >98.5%, St. Louis, Missouri, USA), sodium deoxycholate (Sigma Aldrich, >98%, St. Louis, Missouri, USA), chromium (III) chloride hexahydrate (Sigma Aldrich, >96%, St. Louis, Missouri, USA), and zinc chloride (PanReac, Barcelona, Spain) were used as received.

3.2. Synthesis of LDHs

The synthesis of LDHs was carried out by a conventional co-precipitation procedure. It consisted of mixing 0.0150 moles of ZnCl_2 and 0.0075, 0.0050 or 0.0038 moles of $\text{CrCl}_3 \cdot 6\text{H}_2\text{O}$ (i.e., Zn:Cr ratio equal to 2, 3 and 4) in 150 mL of deionized water and then slowly dropping it on 500 mL of deionized water at 60°C under vigorous stirring for 2 h. At the same time, 1 M NaOH solution was also slowly added to keep $\text{pH} = 9.5$. The suspension obtained was aged at 80°C for 24 h. Then, it was filtered and the solid was washed with 2 L of deionized water to obtain the materials denoted LDH2-Cl, LDH3-Cl and LDH4-Cl.

LDHs with intercalated GQDs, SDS and SDC were synthesized using the previously mentioned approach. The salt mixture (0.0150 moles of ZnCl_2 and 0.0050 moles of $\text{CrCl}_3 \cdot 6\text{H}_2\text{O}$) was slowly added to either a suspension, previously sonicated for 90 min, of 1.0 g GQDs, 5.0 g of SDS (0.0170 moles) [77] or 4.1 g of SDC (0.1000 moles) [65] in 500 mL of deionized water. The addition time was 2 h and the LDH synthesis was carried out at $\text{pH} = 9.5$. Three materials, named LDH3-GQD, LDH3-SDS and LDH3-SDC, were obtained. GQDs were synthesized pyrolyzing 2 g of citric acid at 200°C during 30 min. Citric acid was liquefied, acquiring a gel-like appearance and the color changed to orange [94]. GQD stability in water was studied by zeta-potential distribution measurements in a Zetasizer ZSP analyzer (Malvern, UK). Zeta potential of GQDs at $\text{pH} 9\text{--}10$ was ca. -15 mV (Figure S5).

3.3. Characterization

Zn and Cr contents and Zn/Cr ratio in LDHs were determined by inductively coupled plasma mass spectrometry (ICP-MS) NexION 350X, Perkin Elmer (Waltham, Massachusetts, USA). Elemental analysis results were obtained by combustion of 100 mg of material performed on a LECO TRUSPEC CN carbon (Madrid, Spain). X-ray powder diffraction (XRD) patterns were collected over the 2θ range $1\text{--}80^\circ$ in a Bruker D8 Discover A25 diffractometer using $\text{Cu K}\alpha$ radiation (Billerica, MA, USA). Crystallite size was calculated according to the Scherrer equation, $D_{\text{hkl}} = R (\lambda / \beta \cos\theta)$, where R is the Scherrer number (0.89), λ is the incident X-ray wavelength (0.154 nm), β is the peak width at half height (rad) and θ is the Bragg angle. Raman spectra were acquired in a Renishaw Raman instrument (Wotton-under-Edge, UK) with green laser light (532 nm) over the wavenumber range $150\text{--}4000 \text{ cm}^{-1}$. FT-IR measurements were carried out on a Bruker Tensor 37 ATR-equipped spectrometer (Billerica, MA, USA) over the wavenumber range $500\text{--}4000 \text{ cm}^{-1}$. TEM and HRTEM were performed using a Thermo Fisher FEI Talos F200i S/TEM microscope (Waltham, MA, USA) operating at 200 kV. STEM mode using the high-angle annular dark field (HAADF) detector was also carried out, providing Z contrast imaging. Moreover, elemental mapping was carried out using energy-dispersive X-ray spectroscopy (EDS). Particle size data were obtained in a Hydro 2000 sm laser diffraction analyzer (Malvern Instruments, Worcestershire, UK) using water as dispersant. Nitrogen adsorption-desorption isotherms were obtained in a Micromeritics ASAP 2420 system (Norcross, Georgia, USA) at -196°C . Samples were outgassed at 70°C before the measurements. The Brunauer–Emmett–Teller BET method was used for determining the specific surface area. Ultraviolet visible (UV-vis) diffuse

reflectance spectra were obtained with a Scan UV-vis spectrophotometer, Perkin Elmer Lambda 650 S (Waltham, MA, USA).

3.4. Photocatalytic Tests

All synthesized materials were tested as part of a three-component CO₂ photoreduction system using Ru(bpy)₃²⁺ as photosensitizer and TEOA as sacrificial electron donor. Reactions were carried out in a Penn PhD Photoreactor M2 equipped with an LED light source at $\lambda = 450$ nm. Catalysts (1 mg) were dispersed in a sealed vessel containing 2.85 mL of TEOA/H₂O (2.14 mmol TEOA, triethanolamine) and 8.55 mL of [Ru(bpy)₃]Cl₂·6H₂O (5.02·10⁻³ mmol) in CH₃CN. Before irradiation, the solution was deoxygenated and saturated with CO₂ by bubbling for 15 min. During the reaction, gas samples (100 μ L) were taken at different time intervals using a gas-tight syringe and CO and H₂ were quantified by gas chromatography (Shimadzu GC-2010 Plus) (Kyoto, Japan), using a ShinCarbon ST column (2 m \times 2 mm i.d.) and a barrier discharge ionization detector (BID). Photocatalytic tests were carried out independently in quintuplicate ($n = 5$) and results were expressed as mean values with standard deviations. Another test was performed under N₂ atmosphere to check if the produced CO came from the bubbled CO₂. Selectivity toward CO was calculated using the following equation [45,95]:

$$\text{CO selectivity}(\%) = \frac{2N_{\text{CO}}}{2N_{\text{CO}} + 2N_{\text{H}_2}} \times 100 \quad (5)$$

where N_{CO} and N_{H_2} were CO moles and H₂ moles, respectively.

Apparent quantum yield (AQY) was calculated according to the following expression [33,45]:

$$\text{AQY}(\text{CO})(\%) = \frac{\text{Number of CO molecules} \times 2}{\text{Number of incident photons}} \times 100 \quad (6)$$

Light energy of Penn PhD Photoreactor M2, used to determine AQY values, was measured using a StellarNet blue-wave spectrometer (Tampa, Florida, USA) equipped with an optical fiber.

4. Conclusions

Novel Zn-Cr LDHs materials with intercalated Cl⁻, GQDs, SDS and SDC and different metal ratios have been successfully synthesized by a co-precipitation method. Those Zn-Cr LDHs with GQDs, SDS and SDC as interlayer anions expanded the interlayer space. The specific surface area increased in the samples intercalated with Cl⁻ as the metal ratio increased, being higher in LDH4-Cl. In LDHs with metal ratio 3, those intercalated with GQDs and SDC stood out for their surface area. Pore volume varied analogously. LDH3-Cl, LDH4-Cl and LDH-SDC materials showed smaller particle size and better dispersibility. All samples were evaluated as catalysts in a three-component system for CO₂ reduction to CO under visible light ($\lambda = 450$ nm) using Ru(bpy)₃²⁺ as photosensitizer and TEOA as sacrificial electron donor. To the best of our knowledge, LDHs containing both Zn and Cr metal cations have never been assessed as catalysts for visible light-driven photocatalytic CO₂ reduction processes. All Zn-Cr LDHs catalyzed the reduction of CO₂ to CO, exhibiting remarkable photocatalytic activity and selectivity. While the photocatalytic CO production was higher when using metal ratio 4 in Zn-Cr LDHs with chloride as interlayer anion (7620 μ mol CO g⁻¹), the highest CO selectivity was achieved with LDH3-Cl (90%). As for the study of interlayer anions, LDH3-SDC, which had the largest interlayer space (3.27 nm), relatively low particle size (46 μ m) and moderate surface area (42 m² g⁻¹) compared to the rest of the LDHs, showed excellent performance. After 24 h of visible irradiation, the CO evolved was 10,977 μ mol CO g⁻¹ with a CO selectivity of 88%, the highest reported so far for Zn-Cr LDH photocatalytic systems under similar experimental conditions using the same PS and ED. Thus, CO evolution prevailed over H₂ production, both being competitive reactions.

The present results have shown that several factors influenced the photocatalytic activity of Zr-Cr LDHs. Firstly, a higher metal ratio gave rise to a more efficient catalyst. Secondly, textural properties played a key role, with higher surface area and smaller particle size improving the catalytic performance. Finally, the nature of the interlayer anion in LDHs was also decisive, since it could affect its structure and textural properties, but additionally, it might impact adsorption and diffusion processes. All these factors, separately and jointly, have to be further investigated in order to find more active Zn-Cr LDHs for CO₂ photoreduction under visible light useful for leading to value-added products for the energy sector and for reducing CO₂ levels to mitigate global warming.

Supplementary Materials: The following supporting information can be downloaded at <https://www.mdpi.com/article/10.3390/catal13101364/s1>, Figure S1. (a) TEM images of LDH2-Cl including a SAED pattern and HRTEM imaging (with its corresponding FFT). (b) EDS elemental mapping of LDH2-Cl; Figure S2. (a) TEM images of LDH4-Cl including a SAED pattern and HRTEM imaging (with its corresponding FFT). (b) EDS elemental mapping of LDH4-Cl; Figure S3. Particle size distribution of Zn-Cr LDHs based materials determined by laser diffraction; Figure S4. (a) UV-vis absorption spectra and (b) band gaps of Zn-Cr LDHs based materials; Figure S5. Zeta potential distributions at different pH for GQDs; Figure S6. Hydrogen evolution for the photocatalytic systems: (a) using different metal ratio and chloride as interlayer anion and (b) using different interlayer anion and metal ratio of ca 3; Figure S7. CO selectivity and syngas ratio with error bars for the photocatalytic systems: (a and c) using different metal ratio and chloride as interlayer anion and (b and d) using different interlayer anion and metal ratio of ca 3; Table S1. Apparent quantum yield (CO) for all photocatalytic systems using Zn-Cr LDHs based materials as catalysts irradiated at 450 nm for 24 h; Table S2: Photocatalytic performance of different LDHs materials as catalyst in visible light CO₂ photoreduction systems with Ru(bpy)₃²⁺ as photosensitizer and TEOA as sacrificial electron donor; Figure S8. (a) TEM image including a SAED pattern and HRTEM imaging, (b) EDS elemental mapping and (c) FTIR-ATR spectra of LDH3-SDC after 24 h under visible light irradiation. (d) CO and H₂ evolution and CO selectivity in 3 runs [33–35].

Author Contributions: Conceptualization, D.G.G.-G., D.C., J.A.-G., D.E., J.R.R. and F.J.R.-S.; funding acquisition, D.E., J.R.R. and F.J.R.-S.; investigation, D.G.G.-G. and M.C.-R.; methodology, D.G.G.-G. and D.C.; project administration, D.E., J.R.R. and F.J.R.-S.; resources, D.E., J.R.R. and F.J.R.-S.; supervision, J.R.R. and F.J.R.-S.; validation, D.E., J.R.R. and F.J.R.-S.; writing—original draft, D.G.G.-G., J.A.-G. and M.C.-R.; writing—review and editing, D.G.G.-G., D.C., J.A.-G., M.C.-R., D.E., J.R.R. and F.J.R.-S. All authors have read and agreed to the published version of the manuscript.

Funding: This research was funded by financial support from Ministerio de Ciencia e Innovación for the projects PID2022/142657OB-I00/MCIN/AEI/10.13039/501100011033/FEDER,UE and PDC2022-133973-I00/AEI/10.13039/501100011033 (Mecanismo de Recuperación y Resiliencia de la Unión Europea-Next Generation EU), Consejería de Universidad, Investigación e Innovación from Junta de Andalucía (Project ProyExcel_00492 and FQM-346 group) and Feder Funds.

Data Availability Statement: Data will be available on request.

Acknowledgments: The authors wish to acknowledge the technical staff from the Instituto Químico para la Energía y el Medioambiente (IQUEMA) and Servicio Central de Apoyo a la Investigación (SCAI).

Conflicts of Interest: The authors declare no conflict of interest.

References

1. Megias-Sayago, C.; Bingre, R.; Huang, L.; Lutzweiler, G.; Wang, Q.; Louis, B. CO₂ Adsorption Capacities in Zeolites and Layered Double Hydroxide Materials. *Front. Chem.* **2019**, *7*, 551. [CrossRef]
2. Xu, J.; Liu, X.; Zhou, Z.; Deng, L.; Liu, L.; Xu, M. Surface Defects Introduced by Metal Doping into Layered Double Hydroxide for CO₂ Photoreduction: The Effect of Metal Species in Light Absorption, Charge Transfer and CO₂ Reduction. *Chem. Eng. J.* **2022**, *442*, 136148. [CrossRef]
3. Fang, X.; Chen, C.; Jia, H.; Li, Y.; Liu, J.; Wang, Y.; Song, Y.; Du, T.; Liu, L. Progress in Adsorption-Enhanced Hydrogenation of CO₂ on Layered Double Hydroxide (LDH) Derived Catalysts. *J. Ind. Eng. Chem.* **2021**, *95*, 16–27. [CrossRef]
4. Zhang, Y.; Zhou, T.; Louis, B.; Yu, F.; Dan, J.; Wang, Q. Environmental Benign Synthesis of Lithium Silicates and Mg-Al Layered Double Hydroxide from Vermiculite Mineral for CO₂ Capture. *Catalysts* **2017**, *7*, 105. [CrossRef]

5. Qin, Q.; Wang, J.; Zhou, T.; Zheng, Q.; Huang, L.; Zhang, Y.; Lu, P.; Umar, A.; Louis, B.; Wang, Q. Impact of Organic Interlayer Anions on the CO₂ Adsorption Performance of Mg-Al Layered Double Hydroxides Derived Mixed Oxides. *J. Energy Chem.* **2017**, *26*, 346–353. [[CrossRef](#)]
6. Jerome, M.P.; Alahmad, F.A.; Salem, M.T.; Tahir, M. Layered Double Hydroxide (LDH) Nanomaterials with Engineering Aspects for Photocatalytic CO₂ Conversion to Energy Efficient Fuels: Fundamentals, Recent Advances, and Challenges. *J. Environ. Chem. Eng.* **2022**, *10*, 108151. [[CrossRef](#)]
7. Chung, Y.-C.; Xie, P.-J.; Lai, Y.-W.; Lo, A.-Y. Hollow TiO₂ Microsphere/Graphene Composite Photocatalyst for CO₂ Photoreduction. *Catalysts* **2021**, *11*, 1532. [[CrossRef](#)]
8. Zhang, Z.; Wang, Y.; Cui, G.; Liu, H.; Abanades, S.; Lu, H. Improvement of CO₂ Photoreduction Efficiency by Process Intensification. *Catalysts* **2021**, *11*, 912. [[CrossRef](#)]
9. Dewangan, N.; Hui, W.M.; Jayaprakash, S.; Bawah, A.R.; Poerjoto, A.J.; Jie, T.; Jangam, A.; Hidajat, K.; Kawi, S. Recent Progress on Layered Double Hydroxide (LDH) Derived Metal-Based Catalysts for CO₂ Conversion to Valuable Chemicals. *Catal. Today* **2020**, *356*, 490–513. [[CrossRef](#)]
10. Iguchi, S.; Teramura, K.; Hosokawa, S.; Tanaka, T. Effect of the Chloride Ion as a Hole Scavenger on the Photocatalytic Conversion of CO₂ in an Aqueous Solution over Ni-Al Layered Double Hydroxides. *Phys. Chem. Chem. Phys.* **2015**, *17*, 17995–18003. [[CrossRef](#)]
11. Berardi, S.; Drouet, S.; Francàs, L.; Gimbert-Suriñach, C.; Guttentag, M.; Richmond, C.; Stoll, T.; Llobet, A. Molecular Artificial Photosynthesis. *Chem. Soc. Rev.* **2014**, *43*, 7501–7519. [[CrossRef](#)]
12. Handoko, A.D.; Li, K.; Tang, J. Recent Progress in Artificial Photosynthesis: CO₂ Photoreduction to Valuable Chemicals in a Heterogeneous System. *Curr. Opin. Chem. Eng.* **2013**, *2*, 200–206. [[CrossRef](#)]
13. Mu, W.-H.; Chasse, G.A.; Fang, D.-C. High Level Ab Initio Exploration on the Conversion of Carbon Dioxide into Oxazolidinones: The Mechanism and Regioselectivity. *J. Phys. Chem. A* **2008**, *112*, 6708–6714. [[CrossRef](#)] [[PubMed](#)]
14. Woolcock, P.J.; Brown, R.C. A Review of Cleaning Technologies for Biomass-Derived Syngas. *Biomass Bioenergy* **2013**, *52*, 54–84. [[CrossRef](#)]
15. Venvik, H.J.; Yang, J. Catalysis in Microstructured Reactors: Short Review on Small-Scale Syngas Production and Further Conversion into Methanol, DME and Fischer-Tropsch Products. *Catal. Today* **2017**, *285*, 135–146. [[CrossRef](#)]
16. Rommens, K.T.; Saeys, M. Molecular Views on Fischer–Tropsch Synthesis. *Chem. Rev.* **2023**, *123*, 5798–5858. [[CrossRef](#)]
17. Ali, K.A.; Abdullah, A.Z.; Mohamed, A.R. Recent Development in Catalytic Technologies for Methanol Synthesis from Renewable Sources: A Critical Review. *Renew. Sustain. Energy Rev.* **2015**, *44*, 508–518. [[CrossRef](#)]
18. Baraj, E.; Cihotný, K.; Hlinčík, T. The Water Gas Shift Reaction: Catalysts and Reaction Mechanism. *Fuel* **2021**, *288*, 119817. [[CrossRef](#)]
19. Ng, S.; Lau, M.Y.L.; Ong, W. Engineering Layered Double Hydroxide-Based Photocatalysts Toward Artificial Photosynthesis: State-of-the-Art Progress and Prospects. *Sol. RRL* **2021**, *5*, 2000535. [[CrossRef](#)]
20. Forano, C.; Costantino, U.; Pre, V. Layered Double Hydroxides. In *Developments in Clay Science*; Elsevier: Amsterdam, The Netherlands, 2013; Volume 5, pp. 745–782. ISBN 9780080982588.
21. Ahmed, N.; Shibata, Y.; Taniguchi, T.; Izumi, Y. Photocatalytic Conversion of Carbon Dioxide into Methanol Using Zinc–Copper–M(III) (M = aluminum, Gallium) Layered Double Hydroxides. *J. Catal.* **2011**, *279*, 123–135. [[CrossRef](#)]
22. Prevot, V.; Tokudome, Y. 3D Hierarchical and Porous Layered Double Hydroxide Structures: An Overview of Synthesis Methods and Applications. *J. Mater. Sci.* **2017**, *52*, 11229–11250. [[CrossRef](#)]
23. Aramendía, M.A.; Avilés, Y.; Borau, V.; Luque, J.M.; Marinas, J.M.; Ruiz, J.R.; Urbano, F.J. Thermal Decomposition of Mg/Al and Mg/Ga Layered-Double Hydroxides: A Spectroscopic Study. *J. Mater. Chem.* **1999**, *9*, 1603–1607. [[CrossRef](#)]
24. Kumar, S.; Durrndell, L.J.; Manayil, J.C.; Isaacs, M.A.; Parlett, C.M.A.; Karthikeyan, S.; Douthwaite, R.E.; Coulson, B.; Wilson, K.; Lee, A.F. Delaminated CoAl-Layered Double Hydroxide@TiO₂ Heterojunction Nanocomposites for Photocatalytic Reduction of CO₂. *Part. Part. Syst. Charact.* **2018**, *35*, 1700317. [[CrossRef](#)]
25. Tarhini, A.; Aguirre-Araque, J.; Guyot, M.; Costentin, C.; Rogez, G.; Chardon-Noblat, S.; Prevot, V.; Mousty, C. Behavior of Iron Tetraphenylsulfonato Porphyrin Intercalated into LDH and LSH as Materials for Electrocatalytic Applications. *Electrocatalysis* **2023**, *14*, 111–120. [[CrossRef](#)]
26. Wang, J.; Zhang, Y.; Si, J.; Zhang, W.; Liang, Q.; Li, W.; Jin, B.; Miao, S. Structural Engineering of NiFe-Layered Double Hydroxides and Halloysite Composites for Efficient CO₂ Capture. *Chem. Eng. J.* **2023**, *463*, 142502. [[CrossRef](#)]
27. Gil-Gavilán, D.G.; Cosano, D.; Castillo-Rodríguez, M.; de Miguel, G.; Esquivel, D.; Jiménez-Sanchidrián, C.; Ruiz, J.R.; Romero-Salguero, F.J. Composites of Co-Al Hydrotalcites and Carbon Nanomaterials for Photocatalytic H₂ Production. *Appl. Clay Sci.* **2023**, *238*, 106924. [[CrossRef](#)]
28. Prevot, V.; Touati, S.; Mousty, C. Confined Growth of NiAl-Layered Double Hydroxide Nanoparticles within Alginate Gel: Influence on Electrochemical Properties. *Front. Chem.* **2020**, *8*, 1158. [[CrossRef](#)]
29. Liu, Q.; Han, X.; Park, H.; Kim, J.; Xiong, P.; Yuan, H.; Yeon, J.S.; Kang, Y.; Park, J.M.; Dou, Q.; et al. Layered Double Hydroxide Quantum Dots for Use in a Bifunctional Separator of Lithium–Sulfur Batteries. *ACS Appl. Mater. Interfaces* **2021**, *13*, 17978–17987. [[CrossRef](#)]
30. Chaillot, D.; Bennici, S.; Brendlé, J. Layered Double Hydroxides and LDH-Derived Materials in Chosen Environmental Applications: A Review. *Environ. Sci. Pollut. Res.* **2021**, *28*, 24375–24405. [[CrossRef](#)]

31. Wang, C.; Xu, J.; Zhou, Z. A Mini-Review on CO₂ Photoreduction by MgAl-LDH Based Materials. *Energies* **2022**, *15*, 8117. [[CrossRef](#)]
32. Kumaresan, A.; Yang, S.; Zhao, K.; Ahmad, N.; Zhou, J.; Zheng, Z.; Zhang, Y.; Gao, Y.; Zhou, H.; Tang, Z. Facile Development of CoAl-LDHs/RGO Nanocomposites as Photocatalysts for Efficient Hydrogen Generation from Water Splitting under Visible-Light Irradiation. *Inorg. Chem. Front.* **2019**, *6*, 1753–1760. [[CrossRef](#)]
33. Bai, S.; Wang, Z.; Tan, L.; Waterhouse, G.I.N.; Zhao, Y.; Song, Y.-F. 600 Nm Irradiation-Induced Efficient Photocatalytic CO₂ Reduction by Ultrathin Layered Double Hydroxide Nanosheets. *Ind. Eng. Chem. Res.* **2020**, *59*, 5848–5857. [[CrossRef](#)]
34. Ning, C.; Wang, Z.; Bai, S.; Tan, L.; Dong, H.; Xu, Y.; Hao, X.; Shen, T.; Zhao, J.; Zhao, P.; et al. 650 Nm-Driven Syngas Evolution from Photocatalytic CO₂ Reduction over Co-Containing Ternary Layered Double Hydroxide Nanosheets. *Chem. Eng. J.* **2021**, *412*, 128362. [[CrossRef](#)]
35. Wang, Z.; Xu, S.-M.; Tan, L.; Liu, G.; Shen, T.; Yu, C.; Wang, H.; Tao, Y.; Cao, X.; Zhao, Y.; et al. 600 Nm-Driven Photoreduction of CO₂ through the Topological Transformation of Layered Double Hydroxides Nanosheets. *Appl. Catal. B Environ.* **2020**, *270*, 118884. [[CrossRef](#)]
36. Rojas-Luna, R.; Amaro-Gahete, J.; Gil-Gavilán, D.G.; Castillo-Rodríguez, M.; Jiménez-Sanchidrián, C.; Ruiz, J.R.; Esquivel, D.; Romero-Salguero, F.J. Visible-Light-Harvesting Basolite-A520 Metal Organic Framework for Photocatalytic Hydrogen Evolution. *Microporous Mesoporous Mater.* **2023**, *355*, 112565. [[CrossRef](#)]
37. Wang, K.; Wang, T.; Islam, Q.A.; Wu, Y. Layered Double Hydroxide Photocatalysts for Solar Fuel Production. *Chin. J. Catal.* **2021**, *42*, 1944–1975. [[CrossRef](#)]
38. Iguchi, S.; Hasegawa, Y.; Teramura, K.; Hosokawa, S.; Tanaka, T. Preparation of Transition Metal-Containing Layered Double Hydroxides and Application to the Photocatalytic Conversion of CO₂ in Water. *J. CO₂ Util.* **2016**, *15*, 6–14. [[CrossRef](#)]
39. Sahoo, P.; Ishihara, S.; Yamada, K.; Deguchi, K.; Ohki, S.; Tansho, M.; Shimizu, T.; Eisaku, N.; Sasai, R.; Labuta, J.; et al. Rapid Exchange between Atmospheric CO₂ and Carbonate Anion Intercalated within Magnesium Rich Layered Double Hydroxide. *ACS Appl. Mater. Interfaces* **2014**, *6*, 18352–18359. [[CrossRef](#)]
40. Huang, L.; Wang, J.; Gao, Y.; Qiao, Y.; Zheng, Q.; Guo, Z.; Zhao, Y.; O'Hare, D.; Wang, Q. Synthesis of LiAl₂-Layered Double Hydroxides for CO₂ Capture over a Wide Temperature Range. *J. Mater. Chem. A* **2014**, *2*, 18454–18462. [[CrossRef](#)]
41. Yang, Z.; Wei, J.; Zeng, G.; Zhang, H.; Tan, X.; Ma, C.; Li, X.; Li, Z.; Zhang, C. A Review on Strategies to LDH-Based Materials to Improve Adsorption Capacity and Photoreduction Efficiency for CO₂. *Coord. Chem. Rev.* **2019**, *386*, 154–182. [[CrossRef](#)]
42. Baliarsingh, N.; Mohapatra, L.; Parida, K. Design and Development of a Visible Light Harvesting Ni-Zn/Cr-CO₃²⁻ LDH System for Hydrogen Evolution. *J. Mater. Chem. A* **2013**, *1*, 4236. [[CrossRef](#)]
43. Parida, K.; Mohapatra, L. Recent Progress in the Development of Carbonate-Intercalated Zn/Cr LDH as a Novel Photocatalyst for Hydrogen Evolution Aimed at the Utilization of Solar Light. *Dalton Trans.* **2012**, *41*, 1173–1178. [[CrossRef](#)]
44. Flores-Flores, M.; Luévano-Hipólito, E.; Martínez, L.M.T.; Morales-Mendoza, G.; Gómez, R. Photocatalytic CO₂ Conversion by MgAl Layered Double Hydroxides: Effect of Mg²⁺ Precursor and Microwave Irradiation Time. *J. Photochem. Photobiol. A Chem.* **2018**, *363*, 68–73. [[CrossRef](#)]
45. Jo, W.-K.; Kumar, S.; Tonda, S. N-Doped C Dot/CoAl-Layered Double Hydroxide/g-C₃N₄ Hybrid Composites for Efficient and Selective Solar-Driven Conversion of CO₂ into CH₄. *Compos. Part B Eng.* **2019**, *176*, 107212. [[CrossRef](#)]
46. Bian, X.; Zhang, S.; Zhao, Y.; Shi, R.; Zhang, T. Layered Double Hydroxide-Based Photocatalytic Materials toward Renewable Solar Fuels Production. *InfoMat* **2021**, *3*, 719–738. [[CrossRef](#)]
47. Hong, J.; Zhang, W.; Wang, Y.; Zhou, T.; Xu, R. Photocatalytic Reduction of Carbon Dioxide over Self-Assembled Carbon Nitride and Layered Double Hydroxide: The Role of Carbon Dioxide Enrichment. *ChemCatChem* **2014**, *6*, 2315–2321. [[CrossRef](#)]
48. Zhitova, E.S.; Krivovichev, S.V.; Pekov, I.V.; Yakovenchuk, V.N.; Pakhomovsky, Y.A. Correlation between the D-Value and the M²⁺:M³⁺ Cation Ratio in Mg–Al–CO₃ Layered Double Hydroxides. *Appl. Clay Sci.* **2016**, *130*, 2–11. [[CrossRef](#)]
49. Sakr, A.A.-E.; Zaki, T.; Elgabry, O.; Ebiad, M.A.; El-Sabagh, S.M.; Emara, M.M. Mg-Zn-Al LDH: Influence of Intercalated Anions on CO₂ Removal from Natural Gas. *Appl. Clay Sci.* **2018**, *160*, 263–269. [[CrossRef](#)]
50. Tan, L.; Xu, S.; Wang, Z.; Xu, Y.; Wang, X.; Hao, X.; Bai, S.; Ning, C.; Wang, Y.; Zhang, W.; et al. Highly Selective Photoreduction of CO₂ with Suppressing H₂ Evolution over Monolayer Layered Double Hydroxide under Irradiation above 600 nm. *Angew. Chem.* **2019**, *131*, 11986–11993. [[CrossRef](#)]
51. Wang, X.; Wang, Z.; Bai, Y.; Tan, L.; Xu, Y.; Hao, X.; Wang, J.; Mahadi, A.H.; Zhao, Y.; Zheng, L.; et al. Tuning the Selectivity of Photoreduction of CO₂ to Syngas over Pd/Layered Double Hydroxide Nanosheets under Visible Light up to 600 nm. *J. Energy Chem.* **2020**, *46*, 1–7. [[CrossRef](#)]
52. Jiang, H.; Katsumata, K.-I.; Hong, J.; Yamaguchi, A.; Nakata, K.; Terashima, C.; Matsushita, N.; Miyauchi, M.; Fujishima, A. Photocatalytic Reduction of CO₂ on Cu₂O-Loaded Zn-Cr Layered Double Hydroxides. *Appl. Catal. B Environ.* **2018**, *224*, 783–790. [[CrossRef](#)]
53. Amaro-Gahete, J.; Kaczmarek, A.M.; Esquivel, D.; Jiménez-Sanchidrián, C.; Van Der Voort, P.; Romero-Salguero, F.J. Luminescent Graphene-Based Materials via Europium Complexation on Dipyritylpyridazine-Functionalized Graphene Sheets. *Chem. Eur. J.* **2019**, *25*, 6823–6830. [[CrossRef](#)] [[PubMed](#)]
54. Amaro-Gahete, J.; Benítez, A.; Otero, R.; Esquivel, D.; Jiménez-Sanchidrián, C.; Morales, J.; Caballero, Á.; Romero-Salguero, F.J. A Comparative Study of Particle Size Distribution of Graphene Nanosheets Synthesized by an Ultrasound-Assisted Method. *Nanomaterials* **2019**, *9*, 152. [[CrossRef](#)]

55. Algarra, M.; Moreno, V.; Lázaro-Martínez, J.M.; Rodríguez-Castellón, E.; Soto, J.; Morales, J.; Benítez, A. Insights into the Formation of N Doped 3D-Graphene Quantum Dots. Spectroscopic and Computational Approach. *J. Colloid Interface Sci.* **2020**, *561*, 678–686. [[CrossRef](#)] [[PubMed](#)]
56. Daud, M.; Kamal, M.S.; Shehzad, F.; Al-Harhi, M.A. Graphene/Layered Double Hydroxides Nanocomposites: A Review of Recent Progress in Synthesis and Applications. *Carbon* **2016**, *104*, 241–252. [[CrossRef](#)]
57. Hiragond, C.; Ali, S.; Sorcar, S.; In, S.I. Hierarchical Nanostructured Photocatalysts for CO₂ Photoreduction. *Catalysts* **2019**, *9*, 370. [[CrossRef](#)]
58. Varadwaj, G.B.B.; Nyamori, V.O. Layered Double Hydroxide-and Graphene-Based Hierarchical Nanocomposites: Synthetic Strategies and Promising Applications in Energy Conversion and Conservation. *Nano Res.* **2016**, *9*, 3598–3621. [[CrossRef](#)]
59. Cosano, D.; Esquivel, D.; Romero-Salguero, F.J.; Jiménez-Sanchidrián, C.; Ruiz, J.R. Microwave-Assisted Synthesis of Hybrid Organo-Layered Double Hydroxides Containing Cholate and Deoxycholate. *Mater. Chem. Phys.* **2019**, *225*, 28–33. [[CrossRef](#)]
60. Paušová, Š.; Krýsa, J.; Jirkovský, J.; Forano, C.; Mailhot, G.; Prevot, V. Insight into the Photocatalytic Activity of ZnCr–CO₃ LDH and Derived Mixed Oxides. *Appl. Catal. B Environ.* **2015**, *170–171*, 25–33. [[CrossRef](#)]
61. Hirata, N.; Tadanaga, K.; Tatsumisago, M. Photocatalytic O₂ Evolution from Water over Zn–Cr Layered Double Hydroxides Intercalated with Inorganic Anions. *Mater. Res. Bull.* **2015**, *62*, 1–4. [[CrossRef](#)]
62. Koilraj, P.; Takemoto, M.; Tokudome, Y.; Bousquet, A.; Prevot, V.; Mousty, C. Electrochromic Thin Films Based on NiAl Layered Double Hydroxide Nanoclusters for Smart Windows and Low-Power Displays. *ACS Appl. Nano Mater.* **2020**, *3*, 6552–6562. [[CrossRef](#)]
63. Bai, L.; Xue, N.; Zhao, Y.; Wang, X.; Lu, C.; Shi, W. Dual-Mode Emission of Single-Layered Graphene Quantum Dots in Confined Nanospace: Anti-Counterfeiting. *Nano Res.* **2018**, *11*, 2034–2045. [[CrossRef](#)]
64. Ahmed, A.A.A.; Talib, Z.A.; Hussein, M.Z. Influence of Sodium Dodecyl Sulfate Concentration on the Photocatalytic Activity and Dielectric Properties of Intercalated Sodium Dodecyl Sulfate into Zn–Cd–Al Layered Double Hydroxide. *Mater. Res. Bull.* **2015**, *62*, 122–131. [[CrossRef](#)]
65. Wu, X.; Wang, S.; Du, N.; Zhang, R.; Hou, W. Facile Synthesis of Deoxycholate Intercalated Layered Double Hydroxide Nanohybrids via a Coassembly Process. *J. Solid State Chem.* **2013**, *203*, 181–186. [[CrossRef](#)]
66. EL Mersly, L.; El Mouchtari, E.M.; Moujahid, E.M.; Forano, C.; El Haddad, M.; Briche, S.; Alaoui Tahiri, A.; Rafqah, S. ZnCr-LDHs with Dual Adsorption and Photocatalysis Capability for the Removal of Acid Orange 7 Dye in Aqueous Solution. *J. Sci. Adv. Mater. Devices* **2021**, *6*, 118–126. [[CrossRef](#)]
67. Pavel, O.D.; Șerban, A.; Zăvoianu, R.; Bacalum, E.; Birjega, R. Curcumin Incorporation into Zn₃Al Layered Double Hydroxides—Preparation, Characterization and Curcumin Release. *Crystals* **2020**, *10*, 244. [[CrossRef](#)]
68. Tichit, D.; Lorret, O.; Coq, B.; Prinetto, F.; Ghiotti, G. Synthesis and Characterization of Zn/Al and Pt/Zn/Al Layered Double Hydroxides Obtained by the Sol–Gel Method. *Microporous Mesoporous Mater.* **2005**, *80*, 213–220. [[CrossRef](#)]
69. Zhang, Y.; Zhang, L.; Hu, L.; Huang, S.; Jin, Z.; Zhang, M.; Huang, X.; Lu, J.; Ruan, S.; Zeng, Y.J. Multifunctional Zn–Al Layered Double Hydroxides for Surface-Enhanced Raman Scattering and Surface-Enhanced Infrared Absorption. *Dalton Trans.* **2019**, *48*, 426–434. [[CrossRef](#)]
70. Zhou, B.; Yang, Y.; Liu, Z.; Wu, N.; Yan, Y.; Wenhua, Z.; He, H.; Du, J.; Zhang, Y.; Zhou, Y.; et al. Boosting Photocatalytic CO₂ Reduction via Schottky Junction with ZnCr Layered Double Hydroxide Nanoflakes Aggregated on 2D Ti₃C₂T_x Cocatalyst. *Nanoscale* **2022**, *14*, 7538–7546. [[CrossRef](#)]
71. Rinawati, M.; Wang, Y.-X.; Huang, W.-H.; Wu, Y.-T.; Cheng, Y.-S.; Kurniawan, D.; Haw, S.-C.; Chiang, W.-H.; Su, W.-N.; Yeh, M.-H. Unraveling the Efficiency of Heteroatom-Doped Graphene Quantum Dots Incorporated MOF-Derived Bimetallic Layered Double Hydroxide towards Oxygen Evolution Reaction. *Carbon* **2022**, *200*, 437–447. [[CrossRef](#)]
72. Islam, M.R.; Guo, Z.; Rutman, D.; Benson, T.J. Immobilization of Triazabicyclodecene in Surfactant Modified Mg/Al Layered Double Hydroxides. *RSC Adv.* **2013**, *3*, 24247. [[CrossRef](#)]
73. Mohapatra, L.; Parida, K.M. Zn–Cr Layered Double Hydroxide: Visible Light Responsive Photocatalyst for Photocatalytic Degradation of Organic Pollutants. *Sep. Purif. Technol.* **2012**, *91*, 73–80. [[CrossRef](#)]
74. Lan, M.; Fan, G.; Yang, L.; Li, F. Significantly Enhanced Visible-Light-Induced Photocatalytic Performance of Hybrid Zn–Cr Layered Double Hydroxide/Graphene Nanocomposite and the Mechanism Study. *Ind. Eng. Chem. Res.* **2014**, *53*, 12943–12952. [[CrossRef](#)]
75. Țucureanu, V.; Matei, A.; Avram, A.M. FTIR Spectroscopy for Carbon Family Study. *Crit. Rev. Anal. Chem.* **2016**, *46*, 502–520. [[CrossRef](#)] [[PubMed](#)]
76. Diao, J.; Wang, T.; Li, L. Graphene Quantum Dots as Nanoprobes for Fluorescent Detection of Propofol in Emulsions. *R. Soc. Open Sci.* **2019**, *6*, 181753. [[CrossRef](#)]
77. Zhang, J.; Xie, X.; Li, C.; Wang, H.; Wang, L. The Role of Soft Colloidal Templates in the Shape Evolution of Flower-like MgAl-LDH Hierarchical Microstructures. *RSC Adv.* **2015**, *5*, 29757–29765. [[CrossRef](#)]
78. Teng, W.; Sun, Z.; Xie, J.; Wang, Z.; Zheng, X.; Tang, B. In-Situ Formation of Amorphous Co–Al–P Layer on CoAl Layered Double Hydroxide Nanoarray as Neutral Electrocatalysts for Hydrogen Evolution Reaction. *Front. Chem.* **2020**, *8*, 552795. [[CrossRef](#)] [[PubMed](#)]
79. Jin, Z.; Cao, Y. Cube Cu₂O Modified CoAl-LDH p-n Heterojunction for Photocatalytic Hydrogen Evolution. *Int. J. Energy Res.* **2021**, *45*, 19014–19027. [[CrossRef](#)]

80. Williams, D.B.; Barry Carter, C. *Transmission Electron Microscopy*, 2nd ed.; Springer: New York, NY, USA, 2009; ISBN 978-0-387-76501-3.
81. Patra, P.P.; Chikkaraddy, R.; Tripathi, R.P.N.; Dasgupta, A.; Kumar, G.V.P. Plasmo-fluidic Single-Molecule Surface-Enhanced Raman Scattering from Dynamic Assembly of Plasmonic Nanoparticles. *Nat. Commun.* **2014**, *5*, 4357. [[CrossRef](#)]
82. Jones, A.R. Light Scattering for Particle Characterization. *Prog. Energy Combust. Sci.* **1999**, *25*, 1–53. [[CrossRef](#)]
83. Che, M.; Bennett, C.O. The Influence of Particle Size on the Catalytic Properties of Supported Metals. In *Advances in Catalysis*; Academic Press: Cambridge, MA, USA, 1989; Volume 36, pp. 55–172.
84. Sing, K.S.W. Reporting Physisorption Data for Gas/Solid Systems with Special Reference to the Determination of Surface Area and Porosity (Recommendations 1984). *Pure Appl. Chem.* **1985**, *57*, 603–619. [[CrossRef](#)]
85. Bouteraa, S.; Saiah, F.B.D.; Hamouda, S.; Bettahar, N. Zn-M-CO₃ Layered Double Hydroxides (M=Fe, Cr, or Al): Synthesis, Characterization, and Removal of Aqueous Indigo Carmine. *Bull. Chem. React. Eng. Catal.* **2020**, *15*, 43–54. [[CrossRef](#)]
86. Sahoo, D.P.; Patnaik, S.; Parida, K. An Amine Functionalized ZnCr LDH/MCM-41 Nanocomposite as Efficient Visible Light Induced Photocatalyst for Cr(VI) Reduction. *Mater. Today Proc.* **2021**, *35*, 252–257. [[CrossRef](#)]
87. Li, P.; Hu, H.; Luo, G.; Zhu, S.; Guo, L.; Qu, P.; Shen, Q.; He, T. Crystal Facet-Dependent CO₂ Photoreduction over Porous ZnO Nanocatalysts. *ACS Appl. Mater. Interfaces* **2020**, *12*, 56039–56048. [[CrossRef](#)]
88. Sayed, M.; Xu, F.; Kuang, P.; Low, J.; Wang, S.; Zhang, L.; Yu, J. Sustained CO₂-Photoreduction Activity and High Selectivity over Mn, C-Codoped ZnO Core-Triple Shell Hollow Spheres. *Nat. Commun.* **2021**, *12*, 4936. [[CrossRef](#)]
89. Wang, Y.; Fan, G.; Wang, S.; Li, Y.; Guo, Y.; Luan, D.; Gu, X.; Lou, X.W. (David) Implanting CoO_x Clusters on Ordered Macroporous ZnO Nanoreactors for Efficient CO₂ Photoreduction. *Adv. Mater.* **2022**, *34*, 2204865. [[CrossRef](#)]
90. Stanley, P.M.; Su, A.Y.; Ramm, V.; Fink, P.; Kimna, C.; Lieleg, O.; Elsner, M.; Lercher, J.A.; Rieger, B.; Warnan, J.; et al. Photocatalytic CO₂-to-Syngas Evolution with Molecular Catalyst Metal-Organic Framework Nanozymes. *Adv. Mater.* **2023**, *35*, 2207380. [[CrossRef](#)]
91. Wang, S.; Yao, W.; Lin, J.; Ding, Z.; Wang, X. Cobalt Imidazolate Metal-Organic Frameworks Photosplit CO₂ under Mild Reaction Conditions. *Angew. Chem. Int. Ed.* **2014**, *53*, 1034–1038. [[CrossRef](#)]
92. Rojas-Luna, R.; Castillo-Rodríguez, M.; Ruiz, J.R.; Jiménez-Sanchidrián, C.; Esquivel, D.; Romero-Salguero, F.J. Ru- and Ir-Complex Decorated Periodic Mesoporous Organosilicas as Sensitizers for Artificial Photosynthesis. *Dalton Trans.* **2022**, *51*, 18708–18721. [[CrossRef](#)]
93. Gao, C.; Chen, S.; Wang, Y.; Wang, J.; Zheng, X.; Zhu, J.; Song, L.; Zhang, W.; Xiong, Y. Heterogeneous Single-Atom Catalyst for Visible-Light-Driven High-Turnover CO₂ Reduction: The Role of Electron Transfer. *Adv. Mater.* **2018**, *30*, 1704624. [[CrossRef](#)]
94. Dong, Y.; Shao, J.; Chen, C.; Li, H.; Wang, R.; Chi, Y.; Lin, X.; Chen, G. Blue Luminescent Graphene Quantum Dots and Graphene Oxide Prepared by Tuning the Carbonization Degree of Citric Acid. *Carbon* **2012**, *50*, 4738–4743. [[CrossRef](#)]
95. Navarro, M.; Sain, S.; Wünschek, M.; Pichler, C.; Romero-Salguero, F.J.; Esquivel, D.; Roy, S. Solar Driven CO₂ Reduction with a Molecularly Engineered Periodic Mesoporous Organosilica Containing Cobalt Phthalocyanine. *Nanoscale* **2023**, *15*, 2114–2121. [[CrossRef](#)] [[PubMed](#)]

Disclaimer/Publisher's Note: The statements, opinions and data contained in all publications are solely those of the individual author(s) and contributor(s) and not of MDPI and/or the editor(s). MDPI and/or the editor(s) disclaim responsibility for any injury to people or property resulting from any ideas, methods, instructions or products referred to in the content.